

# A Time-Spectral Method for Overlapping Meshes

Joshua I. Leffell\*

Stanford University, Stanford, CA 94305

Scott M. Murman<sup>†</sup> and Thomas H. Pulliam<sup>‡</sup>

NASA Ames Research Center, Moffett Field, CA 94035

Overset and Cartesian solvers have traditionally been employed to efficiently resolve unsteady flows with conventional time-marching methods. Temporal pseudospectral schemes have demonstrated the ability to dramatically reduce the computational effort required to simulate the important subclass of time-periodic phenomena. Incorporation of the Time-Spectral method within these approaches is desirable, but direct application is infeasible. Relative motion in an overset framework introduces the dynamic blanking of spatial nodes which move interior to the impermeable boundaries of solid bodies; the solution at these nodes is therefore undefined over specific intervals of time. This proves problematic for the conventional Time-Spectral approach, as it expands the temporal variation at every node as an infinitely-supported Fourier series. An extension of the Time-Spectral method is outlined that treats the solution at dynamically-blanked nodes in an alternative manner. The standard Fourier differentiation operator and differentiation operators derived from barycentric rational interpolants are applied in tandem providing a hybrid Time-Spectral scheme capable of consistently resolving relative motion. The proposed scheme is applied to the cases of high-amplitude and high-frequency plunging airfoils, and the results compared against corresponding simulations obtained with a traditional time marching scheme. The results demonstrate that the hybrid scheme mirrors the performance of the conventional Time-Spectral method, and monotonically converges to corresponding high-resolution, time-accurate simulations with increasing temporal nodes.

## Nomenclature

$\mathcal{D}_N$	Differentiation operator
$\tilde{u}_k$	$k$ th frequency component of u-vector
$a$	Plunging amplitude
$c$	Chord length
$c_d$	Sectional drag coefficient
$d$	Barycentric rational interpolant approximation order
$D_N$	Global temporal differentiation operator
$d_{\max}$	Barycentric rational interpolant approximation order limit
$h$	Nondimensional plunging amplitude, $h = a/c$
$i$	Imaginary unit, $\sqrt{-1}$
$I_N$	Interpolation operator
$K$	Number of temporal modes, $K = (N - 1)/2$
$k$	Reduced frequency, $k = \omega c/V_\infty$
$M$	Mach number
$N$	Number of temporal degrees of freedom
$N_Q$	Number of conserved quantities
$N_{SD}$	Number of spatial dimensions
$Re$	Reynolds number
$St$	Strouhal number, $St = kh$
$T$	Temporal period
$t$	Physical time

## Greek Letters

$\delta_x$	General finite-difference operator in the $x$ -direction
$\omega$	Fundamental frequency
$\phi_k$	Basis function corresponding to the $k$ th mode or node
$\psi_k$	Test function corresponding to the $k$ th mode or node
$\tau$	Pseudotime

\*Currently Aerospace Engineer with U.S. Army Aviation Development Directorate, NASA Ames Research Center, Mailstop 215-1, Moffett Field, CA 94035. AIAA Member, [Joshua.I.Leffell@nasa.gov](mailto:Joshua.I.Leffell@nasa.gov)

<sup>†</sup>Research Scientist, NASA Modeling and Simulations Branch, NASA Ames Research Center, Mailstop 258-5, Moffett Field, CA 94035, AIAA Member, [Scott.M.Murman@nasa.gov](mailto:Scott.M.Murman@nasa.gov)

<sup>‡</sup>Senior Research Scientist, NASA Modeling and Simulations Branch, NASA Ames Research Center, Mailstop 258-2, Moffett Field, CA 94035, AIAA Associate Fellow, [Thomas.H.Pulliam@nasa.gov](mailto:Thomas.H.Pulliam@nasa.gov)

## Superscripts

$n$	Physical time index
$s$	Iteration index

## Subscripts

$\infty$	Freestream value
----------	------------------

## I. Introduction

FORCED periodic flows arise in a broad range of aerodynamic applications such as rotorcraft, turbomachinery, and flapping-wing configurations. The standard procedure for simulating such flows involves advancing the unsteady governing equations forward in time long enough for the initial transient to exit the computational domain and ultimately to achieve a statistically stationary flow. It is often necessary to simulate several periods of motion to accomplish this task, making unsteady design optimization prohibitively expensive for many realistic problems. An effort to reduce the computational expense of these calculations led to the development of the Harmonic Balance (HB) method [1, 2], which capitalizes on the periodic nature of the solution while maintaining the ability to resolve nonlinearities inherent in the underlying physics. This approach exploits the fact that time-periodic flow, while varying in the time domain, is invariant in the frequency domain. Expanding the temporal variation at each spatial node as a truncated Fourier series transforms the unsteady governing equations into a coupled set of steady equations in integer harmonics that can be tackled with the acceleration techniques commonly afforded to steady-state flow solvers. Other similar Fourier pseudospectral approaches, such as the Nonlinear Frequency Domain (NLFD) [3, 4, 5], Reduced Frequency [6], and Time-Spectral (TS) [7, 8, 9] methods, were also developed.

Temporal Fourier pseudospectral methods have demonstrated marked success in reducing the computational costs associated with simulating forced periodic flows [4]. In such an approach, the solutions at  $N$  equispaced time instances are coupled through an infinitely-supported temporal differentiation operator. The trigonometric representation of periodic phenomena provides spectral convergence as the

number of resolved harmonics,  $K$ , and correspondingly, the number of time samples,  $N = 2K + 1$ , increases. The spectral convergence rate of Fourier methods is superior to the algebraic convergence rates associated with traditional time-marching schemes for unsteady calculations, implying that a given level of accuracy can be achieved with significantly fewer temporal degrees of freedom [10]. Some approaches iterate the equations in the frequency domain while others operate entirely in the time domain to simplify the process of augmenting this capability within existing flow solvers. However, each approach harnesses the underlying steady solution in the frequency domain.

Cartesian and overlapping grid methodologies are versatile techniques capable of handling complex-geometry configurations with relative motion between components, and are commonly used for practical engineering applications. The combination of the Time-Spectral approach with this general capability has the potential of providing an enabling design and analysis tool. In an arbitrary moving-body scenario for overset or Cartesian approaches, a Lagrangian body moves relative to a fixed Eulerian mesh (or another Lagrangian mesh). Mesh points interior to solid bodies are removed (*blanked* or *cut*), leaving a *hole* in the background mesh. Blanked mesh points are excluded from the computational domain through which the governing equations are solved, rendering the solution at such nodes as undefined. In general, such grid points undergo *dynamic blanking* where they are blanked for only a fraction of time and active otherwise. Dynamically-blanked nodes lack a complete set of time samples, preventing direct application of the Time-Spectral approach due to the infinite support of the complex exponential basis functions of the Fourier series, upon which the method is based. Murman [6] incorporated a temporal pseudospectral approach within a Cartesian solver with rigid domain motion, wherein the hole cutting remained fixed. Similarly, Thomas et al. [11, 12] and Custer [13] applied the method to the NASA overset OVERFLOW solver with static hole cutting. Blanc et al. [9] implemented an iterative procedure to eliminate dynamically-blanked nodes, if possible, to facilitate the use of the standard Time-Spectral method on dynamic overset grids. Soucy et al. [14] avoided dynamically-blanked nodes by extending the near-body grids such that they envelop the solid body at all time instances. These approaches prove worthy for simple configurations but are not general solutions for the case of arbitrary relative motion. Mavriplis et al. [15] demonstrated a general approach to treat dynamically-blanked nodes by applying Laplacian smoothing to populate blanked data using the solution on the boundaries of hole cuts. In the current work, a hybrid Time-Spectral scheme capable of consistently treating dynamically-blanked nodes resulting from general relative motion between overset grids is developed and implemented within NASA's OVERFLOW solver.

Background on the Time-Spectral method and overset grid technology is presented in §II, providing context for §III, which expounds on the difficulty of applying the Time-Spectral method within the overset framework for arbitrary relative motion. Section III also introduces a strategy to resolve overset relative motion within the Time-Spectral methodology. Section IV first describes NASA's existing OVERFLOW solver and then outlines the augmented Time-Spectral OVERFLOW solver; memory and computational overhead with respect to the steady-state solver is addressed. Various numerical experiments are presented in §V to demonstrate the viability of the proposed approach, including both inviscid, high-amplitude and laminar high-frequency oscillating airfoils.

## II. Background

Brief descriptions of the conventional Time-Spectral method and overset grid methodology are provided for context of the topic and proposed solution strategy.

### The Time-Spectral Method

The standard Time-Spectral method is derived as a Fourier collocation scheme [16, 17] for a time-periodic solution,  $u$ , to a representative semi-discretized partial differential equation (PDE); the discrete spatial residual operator,  $\mathbf{R}(u)$ , is free to be of linear or nonlinear form.

$$\frac{d}{dt}u(\mathbf{x}, t) + \mathbf{R}(u(\mathbf{x}, t)) = 0 \quad (1)$$

The solution is assumed periodic in time a priori, such that  $u(\mathbf{x}, t + T) = u(\mathbf{x}, t)$  for a given period  $T$ . It is therefore advantageous to express the solution at every point in space,  $\mathbf{x}$ , as a Fourier series whose basis functions,  $\phi_k(t) = e^{i\omega kt}$ , are the complex exponentials in integer harmonics of the fundamental frequency,  $\omega = 2\pi/T$ , which naturally satisfy periodicity.

$$u(\mathbf{x}, t) = \sum_{k=-\infty}^{\infty} \tilde{u}_k(\mathbf{x}) \phi_k(t) \quad (2)$$

In order to solve a finite-dimensional problem, and also because the bulk of energy in forced periodic flows is often concentrated in the lower frequencies, Eq. (2) is truncated to  $N = 2K + 1$  terms, which retains  $K$  modes in the approximate solution,  $u_N$ .

$$u_N(\mathbf{x}, t) = I_N u = \sum_{k=-K}^K \tilde{u}_k(\mathbf{x}) \phi_k(t) \quad (3)$$

The Method of Weighted Residuals is applied to approximate the solution to PDEs by minimizing a discrete residual,  $R_N$ , of Eq. (1).

$$R_N(\mathbf{x}, t) = \frac{\partial}{\partial t}u_N(\mathbf{x}, t) + \mathbf{R}(u_N(\mathbf{x}, t)) \quad (4)$$

This approach requires that  $R_N$  integrates to zero against an appropriate set of test functions,  $\psi$ , over the period [18].

$$(R_N, \psi_n)_w = \int_0^T R_N \psi_n w dt = 0, \quad n \in \{0, \dots, N-1\} \quad (5)$$

The choice of weight and test functions,  $w = 1$  and  $\psi_n = \delta(t - t_n)$ , respectively, defines a collocation scheme as it eliminates the discrete residual at each of the  $N$  collocation points,  $t_n$ .

$$\frac{d}{dt}u_N(\mathbf{x}, t_n) + \mathbf{R}(u_N(\mathbf{x}, t_n)) = 0, \quad n \in \{0, \dots, N-1\} \quad (6)$$

Because the temporal basis functions are the complex exponential functions, the collocation points are distributed uniformly over the period,  $t_n = nT/N$ .

The temporal derivative in Eq. (6) is evaluated by analytically differentiating the truncated Fourier series in Eq. (3).

$$\frac{d}{dt}u_N(\mathbf{x}, t) = \sum_{k=-K}^K i\omega k \tilde{u}_k(\mathbf{x}) e^{i\omega kt} \quad (7)$$

The spatially-varying Fourier coefficients,  $\tilde{u}_k(\mathbf{x})$ , are determined by application of the *discrete* Fourier transform (DFT) to the solution values at the  $N$  collocation points,  $u_N^n(\mathbf{x}) = u_N(\mathbf{x}, t_n)$ .

$$\tilde{u}_k(\mathbf{x}) = \frac{1}{N} \sum_{j=0}^{N-1} u_N^j(\mathbf{x}) e^{-i\omega kt_j} \quad (8)$$

While application of the DFT results in a pseudospectral method, it enables the direct adoption of spatial operators from existing flow solvers as the spatial residual is evaluated in the time domain. Substitution of  $\tilde{u}_k$  in Eq. (8) into Eq. (7) defines the temporal derivative at a particular time sample,  $t_n$ , as a weighted sum of the solution at every other time sample ( $d_n^n = 0$ ).

$$\frac{d}{dt}u_N^n(\mathbf{x}) = \sum_{k=-K}^K i\omega k \tilde{u}_k(\mathbf{x}) e^{i\omega kt_n} \quad (9)$$

$$= \sum_{j=0}^{N-1} \left( \frac{1}{N} \sum_{k=-K}^K i\omega k e^{i\omega k(t_n - t_j)} \right) u_N^j(\mathbf{x}) \quad (10)$$

$$= \sum_{j=0}^{N-1} d_j^n u_N^j(\mathbf{x}) \quad (11)$$

The time derivative can be evaluated at each collocation point and expressed in matrix form defining the *Fourier interpolation* derivative

operator [19],  $\mathcal{D}_N$ , which acts on the time-history of the solution,  $\mathbf{u}_N(\mathbf{x}) = \{u_N^0(\mathbf{x}), \dots, u_N^{N-1}(\mathbf{x})\}^T$ .

$$\frac{d}{dt} \mathbf{u}_N(\mathbf{x}) = \mathcal{D}_N \mathbf{u}_N(\mathbf{x}) \quad (12)$$

The elements,  $d_j^n$ , of the temporal differentiation operator are included here for  $N$  odd [8].

$$d_j^n = \begin{cases} \frac{\omega}{2} (-1)^{n-j} \csc\left(\frac{\pi(n-j)}{N}\right), & j \neq n \\ 0, & j = n \end{cases} \quad (13)$$

Replacing the analytic temporal derivative in Eq. (6) with the discrete approximation in Eq. (11) results in a steady system of equations spanning both time and space.

$$\sum_{j=0}^{N-1} d_j^n u_N^j + \mathbf{R}(u_N^n) = 0, \quad n \in \{0, \dots, N-1\} \quad (14)$$

A pseudotime continuation is applied to Eq. (14) to facilitate an iterative procedure to drive the system of equations to a satisfactory level of convergence.

$$\frac{d}{d\tau} u_N^n + \sum_{j=0}^{N-1} d_j^n u_N^j + \mathbf{R}(u_N^n) = 0, \quad n \in \{0, \dots, N-1\} \quad (15)$$

The discrete Fourier series  $I_N u = u_N$  in Eq. (3) interpolates the solution at each of the  $N$  time samples and can be used to reconstruct the solution at any point in continuous time upon satisfying Eq. (15).

As previously described, the collocation scheme employs the DFT to enable operation in the time domain. While this avoids the need to develop a frequency-domain spatial residual operator, application of the DFT introduces the possibility for aliasing errors to corrupt the solution when solving nonlinear equations, such as the Navier-Stokes equations governing fluid dynamics [10]. While aliasing errors do not degrade the spectral convergence rate of the discrete Fourier series [20], they can destabilize calculations. Therefore, Spectral Vanishing Viscosity (SVV), in the form originally proposed by Tadmor [21], is applied by adding an artificial temporal viscosity term in the form of a second-degree global differentiation operator that is only active above a certain cutoff frequency, resulting in a *dealised* form of the semi-discretized PDE.

$$\frac{\partial}{\partial t} u_N(\mathbf{x}, t) + \mathbf{R}(u_N(\mathbf{x}, t)) = \epsilon \frac{\partial}{\partial t} \left( \mathcal{Q}_N \frac{\partial}{\partial t} u_N(\mathbf{x}, t) \right) \quad (16)$$

This approach damps the high-frequency modes, attenuating their destabilizing impact on the resolved spectrum. Maday and Tadmor [22] applied the concept to the periodic case using a spectral viscosity operator,  $\mathcal{Q}_N$ , defined as a convolution with a *symmetric viscosity kernel*,  $\mathcal{Q}_N(t)$ . The spectral viscosity operator acts exclusively upon the higher modes by prescribing frequency domain kernel components that are null below a cutoff frequency,  $M$ , and smoothly transition to unity at the highest frequencies. Here, the cutoff frequency is taken as roughly two-thirds the highest mode,  $M = \lfloor \frac{2K}{3} \rfloor$ , with temporal viscosity coefficient,  $\epsilon = \Delta t/K$ . Spectral vanishing viscosity is found to stabilize otherwise unstable or non-convergent calculations as demonstrated in §V for the case of the high-frequency laminar plunging NACA 0012 airfoil where significant content is captured in the high-frequency modes.

### Overset Grid Technology

The chimera grid approach was introduced to facilitate the use of efficient structured-grid algorithms on complex geometries by splitting the computational domain into a system of overlapping meshes [23]. In standard practice, curvilinear, body-fitted grids wrap the solid geometry, e.g. airfoil, and are embedded within a system of background Cartesian grids that span the farfield boundaries. Mesh points interior to the solid bodies are blanked (*cut*) because the equations governing fluid dynamics are invalid. Overset grids, while separate logical entities, must be connected to facilitate communication across their boundary interfaces. This requires overlap regions whose size depends on the

stencil of the numerical scheme. Fringe points are identified on the boundary of the overlap regions and tagged as receiver nodes. The domain connectivity software interpolates the solution from the donor grid in the vicinity of each fringe point in order to define the solution on boundary interfaces. This is repeated on all grids ensuring that every boundary node is either populated with interpolated data from a neighboring zone or is defined through a physical or farfield boundary condition.

In a moving body scenario, grids can either move together rigidly or relative to one another. For the case of rigid motion, where all grids move in unison, the blanking status for all mesh points remains constant in time such that a spatial node whose solution is defined at one time sample has a solution that is defined at every time sample. However, for the case of relative motion, where grids move independently, the blanking status of particular grid points may change over time. Consider the case of a plunging airfoil. A curvilinear near-body grid is used to resolve the geometry of the airfoil and is embedded within a background Cartesian grid spanning the farfield domain. Figure 1 is used to examine the blanking status for the background Cartesian grid for both rigid and relative motion. The background grid is depicted at three time instances, corresponding to the three equispaced time samples associated with a Time-Spectral calculation using a single harmonic ( $N = 3$ ). The blue-colored nodes are unblanked for every time instance and the white region corresponds to the hole cut at the particular time instance. For the case of rigid-body motion, depicted in Fig. 1a, the hole cut remains constant; every node that is unblanked at one time instance is unblanked for all three. This is not true for the case of relative motion depicted in Fig. 1b. Because the airfoil grid moves relative to the stationary background grid, the hole cut trims a different set of nodes at each time instance; some nodes are blanked at one time instance but unblanked at another time instance. These *dynamically-blanked* nodes are colored red in the figure and only contain physically meaningful solution data at a subset of the three time samples.

Herein lies the fundamental difficulty of applying the Time-Spectral approach to an overset solver; complete time histories are not available for every grid point which precludes the ability to uniquely represent the aperiodic solution at dynamically-blanked nodes with a discrete Fourier transform. The infinitely-supported Fourier differentiation operator cannot be employed under such circumstances and therefore, an alternative treatment is sought for such nodes which is the subject of the following section.

## III. Dynamic Hole Cutting and The Hybrid Time-Spectral Method

The fundamental obstacle of extending the Time-Spectral method to overset solvers concerns the nodes that dynamically move in and out of the physical domain due to the relative motion between grids and solid geometry. Such nodes lack a complete time history of  $N$  physical states at the  $N$  equispaced temporal collocation points, rendering the infinitely-supported Fourier differentiation operator, and the standard Time-Spectral method upon which it is based, unsuitable. Thus, an alternative approach is required for representing the solution, and correspondingly its temporal derivative, at the unblanked collocation points at nodes undergoing dynamic hole cutting. Unfortunately, the incompatible Fourier interpolation temporal differentiation operator is the optimal choice for periodic problems, so the primary objective of the current work is to determine an appropriate differentiation operator at such nodes without sacrificing the spectral convergence exhibited by the standard Time-Spectral method.

Figure 2 illustrates the issue at dynamically-blanked nodes for a representative one-dimensional oscillating piston. Fictional solutions in Fig. 2b corresponding to nodes  $a$ ,  $b$  and  $c$  in Fig. 2a demonstrate dynamic hole cutting by the motion of the piston relative to the fixed background Eulerian grid. Node  $a$  never lies within the piston, and therefore its solution is defined over the entire period. The piston blanks node  $b$  briefly and node  $c$  twice. Thus, node  $b$  has a single associated sub-periodic time interval while node  $c$  has two – one each represented by the solid and hashed lines in Fig. 2b. The shaded regions serve to highlight the time over which each node lies outside the physical domain, i.e. inside the impermeable boundary of the piston, lacking a physi-

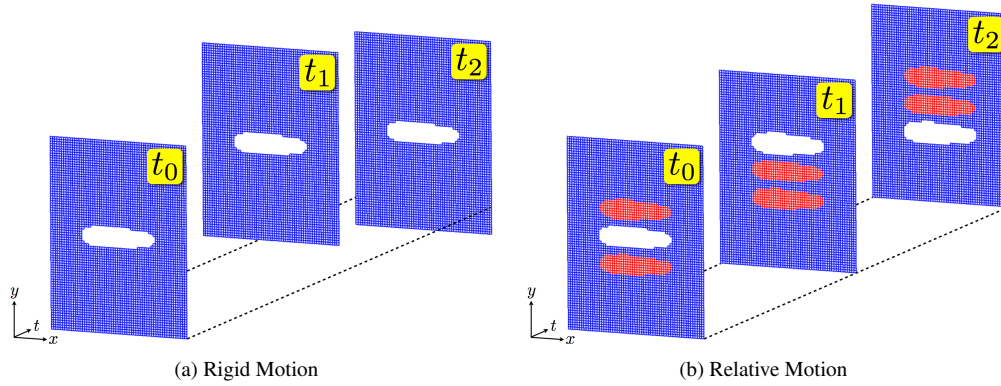


Figure 1: Hole cut at three time instances for a plunging airfoil for both rigid and relative motion. The time instances are defined by  $t_j = jT/3$ ,  $j \in \{0, 1, 2\}$ . For (a) rigid motion, the hole cut remains constant on the background grid. However, for (b) relative motion, the hole cut moves dynamically resulting in spatial nodes (in red) that are only defined for a subset of the global number of time samples and therefore lack complete time histories.

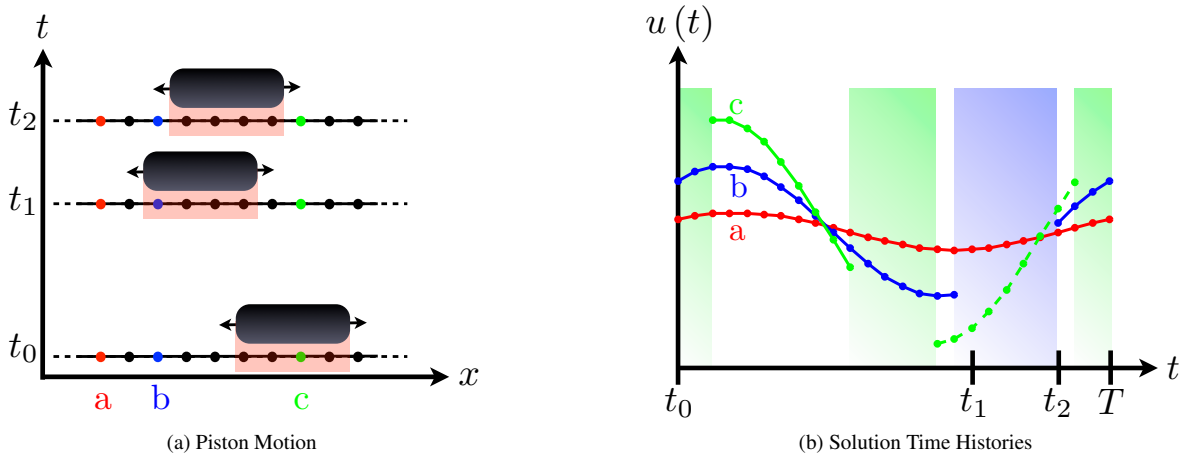


Figure 2: Figurative piston trajectory and solution histories. (a) Position of the piston in space at three time instances. The piston *cuts* nodes  $b$  and  $c$  as it oscillates over the background grid. (b) Intervals of defined solutions for nodes  $a$ ,  $b$  and  $c$ . Shaded regions represent blanked regions through which the solution is undefined for nodes of the corresponding color.

cally meaningful solution. The standard Time-Spectral scheme can be applied to node  $a$ , while special treatment is required for nodes  $b$  and  $c$ .

The objective of the proposed approach is to successfully approximate the solution, and ultimately its temporal derivative, at each dynamically-blanked spatial node. Furthermore, it is critical to maintain equidistant collocation points at dynamically-blanked nodes. One of the more attractive features of the Time-Spectral method is the ability to incorporate its functionality into mature flow solvers in a straightforward manner by leveraging existing spatial operators. Selecting a different distribution of temporal collocation points at dynamically-blanked nodes would require a complete overhaul of the spatial residual operators; spatial neighbors would no longer be guaranteed to be available at the same time instances, therefore requiring costly and potentially ill-conditioned temporal interpolation to evaluate spatial derivatives. Therefore, the distribution of evenly-spaced collocation points is constrained at all grid points, independent of their blanking status.

Overset solvers typically employ a spatial smoothing operation to populate the solution within hole cuts with non zero data in case such points are inadvertently queried. Mavriplis et al. [15] outlined a general Time-Spectral solver for relative motion by taking advantage of this common feature. In this approach, Laplace's equation is solved over the domain of blanked spatial nodes using the data on the hole cut fringe as the boundary condition. This process guarantees that each mesh point has a complete time history, independent of its blanking status. The conventional Time-Spectral differentiation operator is then applied to approximate the temporal derivative. While attractive for its straightforward implementation, the spatial-smoothing approach proves inconsistent; non-physical information provided by an alternative governing equation (Laplace's equation) is propagated into the physical domain via the infinite support of the complex exponential basis functions. While the resulting solution may be smooth, it is dependent upon the arbitrary averaging of the solution through the blanked region. Blanked regions can be of any size and there is no expectation that a spatially-smoothed solution will result in a Fourier expansion that successfully approximates the physically-defined temporal interval of the solution. Consequently, spatial interpolation inhibits the desired temporal convergence with  $N$  [24]. Therefore, alternatives that do not depend on arbitrarily filling data at the blanked nodes were pursued.

Three fundamentally different approaches were considered for treating dynamically-blanked nodes, and there exist several potential candidate treatments within each category. The first approach is global in nature and attempts to fit a basis of complex exponentials to the available data from all physically-defined nodes; the two candidate treatments for this approach result in an overdetermined system (least-squares) and an underdetermined system (least-norm). The second fundamental approach is local in nature and partitions the time history at dynamically-blanked mesh points into intervals of consecutively-unblanked nodes. The solution within each interval is expanded independently in a local basis that avoids extending the solution to blanked time samples. A selection of candidate treatments were surveyed including both a periodization strategy that fits complex exponentials to data within each interval and a bounded interval approach using compactly-supported operators. The third and final approach combines elements of the first two using a mixed representation; a global basis resolves the bulk characteristics of the solution and a local correction recovers an interpolation scheme consistent with the Time-Spectral method. The local approach on a bounded interval ultimately proved most successful for the problems investigated but all of the aforementioned approaches are detailed by Leffell [25].

A natural approach to avoid corruption from unphysical data is to relinquish the global description of the solution by splitting the temporal domain into independent sub-periodic intervals. For a local description of the solution, time histories for dynamically-blanked spatial nodes are partitioned into intervals of consecutively-unblanked temporal collocation points. Independent temporal bases are used to represent the solution within each partition and differentiated accordingly. Global temporal support is thus abandoned; however, this approach is consistent with the physics of disjoint domains separated by an impermeable boundary.<sup>a</sup>

<sup>a</sup>This approach does introduce a potential hazard for rapidly blanking nodes,

Several candidates were evaluated to determine an appropriate basis on a bounded interval of consecutively-defined time samples. One option is to compute derivatives with finite differences or a localized differentiable basis such as wavelets. However, compact bases offer limited accuracy [28] and wavelet differentiation requires special treatment at non-periodic interval boundaries [29]. Another option is temporal extrapolation that populates the undefined region using data from the physical portion of the time signal which can then be differentiated with the conventional Fourier-based operator. Examples of this approach, such as Fourier continuation, which extrapolates a non-periodic function into a periodic function on a larger domain [30, 31, 32], and compressed sampling, which requires  $L_1$  minimization to solve an underdetermined system [33], are either too costly or lack the requisite robustness for this application; some results using the least-squares approach are included for comparison. Orthogonal polynomials (e.g. Chebyshev) offer spectrally-accurate interpolation and differentiation on aperiodic domains, but they are severely ill-conditioned on equispaced samples; approximation using orthogonal polynomials on equispaced data often exhibit violent oscillations on interval boundaries referred to as Runge's phenomenon [34]. Endpoint clustering resolves this issue but violates the prescribed constraint of uniform time sampling in the current application. A least-squares projection of orthogonal polynomials onto equispaced data is more stable, but results in an overdetermined system whose projection does not interpolate the solution data. Barycentric rational interpolants provide a viable alternative for the difficult problem of function approximation on equispaced data [35]. Bos et al. [36] demonstrated their superior approximation and differentiation properties on equidistant nodes over conventional orthogonal polynomials. Efforts to explore rational interpolants and their utility as a pseudospectral basis for spectral collocation methods include but are not limited to [37, 38, 39, 40]. In the approach ultimately adopted, solutions across each non-periodic interval are expanded in a basis of rational interpolants and differentiated accordingly. Fully periodic intervals are still expanded and differentiated in the Fourier basis, resulting in a hybrid approach employing the optimal basis available.

Baltensperger and Berrut [41] define the rational interpolant,  $r(x)$ , approximating the function  $f$  in barycentric form

$$r(x) = \frac{\sum_{k=0}^N \frac{w_k}{x-x_k} f(x_k)}{\sum_{k=0}^N \frac{w_k}{x-x_k}} \quad (17)$$

and its corresponding differentiation operator,  $\mathcal{D}_N$ , such that  $\frac{d}{dx} r = \mathcal{D}_N r$

$$d_k^j = \begin{cases} \frac{w_k}{w_j} \frac{1}{(x_j-x_k)} & \text{if } j \neq k \\ -\sum_{i=0, i \neq k}^N d_i^j & \text{if } j = k \end{cases} \quad (18)$$

where  $r_k = r(x_k) = f(x_k)$ . The interpolation can be reformulated as a weighted sum of nodal basis functions,  $\phi_k(x)$ , with coefficients that are equivalent to the function value at each node,  $f_k = f(x_k)$ .

$$I_N f(x) = \sum_{k=0}^N f_k \phi_k(x), \quad \text{with } \phi_k(x) = \frac{\frac{w_k}{x-x_k}}{\sum_{k=0}^N \frac{w_k}{x-x_k}} \quad (19)$$

The barycentric rational basis functions nodally interpolate the solution data,  $\phi_k(x_j) = \delta_{jk}$ , implying discrete orthogonality at the sample points.

While similar in form to the Lagrange interpolant, a key distinction of the barycentric rational interpolant is in how the weights,  $w_k$ , are defined. The Lagrange interpolant is constrained to pass through  $N+1$  points as a polynomial of degree  $N$ . In contrast, while the rational interpolant passes through the data, it is not forced to do so as

i.e. if a node alternates between blanked and unblanked at every consecutive time instance, the solution will be considered constant in time at each of the nodes and therefore the time derivative will be approximated as zero universally. This may prove problematic, but perhaps such situations would require higher temporal resolution to resolve the high-frequency motion, suggesting the incorporation of temporal adaptation [26, 27]

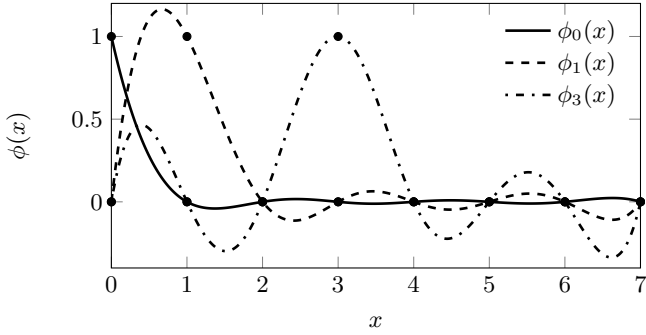


Figure 3: Barycentric rational interpolant basis functions  $\phi_0(x)$ ,  $\phi_1(x)$  and  $\phi_3(x)$  corresponding to nodes 0, 1 and 3, respectively, for approximation order  $d = 3$  over 8 equispaced sample points.

a polynomial of degree  $N$ . This relaxation helps to alleviate spurious oscillations at the endpoints of equispaced nodes associated with the traditional Lagrange or Chebyshev polynomial bases, while retaining powerful interpolation and differentiation properties.

Floater and Hormann [42] derived weights that provide an approximation order  $d + 1$  while avoiding poles. The weights,  $w_k$ , control the accuracy and stability properties of the rational interpolant, which is a blend of polynomials of degree  $d$ . Weights guaranteeing an absence of poles are defined for  $N + 1$  samples

$$w_k = (-1)^{k-d} \sum_{i \in J_k} \prod_{j=i, j \neq k}^{i+d} \frac{1}{|x_k - x_j|} \quad (20)$$

where

$$I := \{0, 1, \dots, N - d\} \text{ and } J_\alpha := \{i \in I : \alpha - d \leq i \leq \alpha\}$$

for the desired approximation order,  $d$ . For uniform nodes, the resulting weights can be scaled to integer values without modifying the interpolant.

$$w_k = (-1)^{k-d} \sum_{i \in J_k} \binom{d}{k-i} \quad (21)$$

Readers are directed to the derivation in [42] for additional detail. Figure 3 illustrates three basis functions corresponding to the first, second and fourth nodes with approximation order  $d = 3$  over 8 equispaced sample points with the values highlighted at the nodal points.

The application of barycentric rational interpolation to a representative signal taken from the inviscid plunging airfoil case in §V is demonstrated in Fig. 4 (with approximation order limit,  $d_{\max} = 1$ ). For the first case, shown in Fig. 4a, only nine global collocation points are used with eight collocation points remaining unblanked. Note that the algorithm does not identify two interruptions in the continuous time signal with nine time instances because it does not sample in the second of the two *continuous* blanked regions; it therefore represents the solution spanning the eight unblanked nodes in a single basis (Figure 4a). In the second example depicted in Fig. 4b, twenty-six out of the thirty-three global collocation points remain unblanked. Using  $N = 33$  global collocation points does, in fact, result in two distinct intervals that are each represented by independent barycentric rational interpolants. Residual plots in Figs. 4c and 4d demonstrate excellent agreement with the continuous segments of the solution away from interval boundaries. It may be beneficial to detect the blanked region for the case of  $N = 9$ . This would require a potentially expensive preprocessor using a predetermined or user-supplied sampling granularity to cycle through the motion, recording the dynamically-blanked boundaries at a finer resolution. Using this information, the solution in Fig. 4a would also be partitioned and not interpolated through undefined regions.

In the Time-Spectral method, differentiation of the expansion is required and therefore the accuracy of each candidate in this endeavor must be assessed. Here, the differentiation performance of the rational

interpolant is compared to that of finite differences, the Fourier differential operator (generally optimal for periodic functions), the Chebyshev differentiation operator on clustered Chebyshev nodes (generally optimal for non-periodic functions) and differentiation operators derived from cubic splines with two different boundary conditions (Natural and Not-a-Knot). An even-odd harmonic function,  $f(x) = 1 + \cos(\pi x) + \sin(\pi x)$ , and Runge's function,  $f(x) = 1/(1 + 25x^2)$ , are differentiated by a selection of the aforementioned methods. Convergence of differentiation error,  $e = \|\frac{df}{dx} - \mathcal{D}_N f\|_2$ , versus  $N$  is plotted in Fig. 5 for the harmonic function and Fig. 6 for Runge's function. The rational interpolant approximation order,  $d = \min(\lfloor \frac{N-1}{2} \rfloor, d_{\max})$ , is defined for different values of  $d_{\max}$ . Fourier differentiation exhibits roundoff error for the harmonic function with increased  $N$  and offers poor convergence for Runge's function. Chebyshev differentiation demonstrates spectral convergence for both functions (albeit delayed for Runge's function in contrast to the harmonic function) and boundary condition selection makes a significant difference for spline-based differentiation. While the rational interpolant-based differentiation operator demonstrates spectral-like convergence for  $d_{\max} \in \{8, 16\}$  on the smooth harmonic function, it diverges for those values of  $d$  for small  $N$  in the case of Runge's function. Taking the best rational result for every  $N$  in the Runge's function example produces spectral-like convergence (even outpacing the Chebyshev convergence) reinforcing the importance of selecting an appropriate value for  $d$ . Using a lower value of  $d$  is associated with higher compactness, and is therefore more successful for high-frequency functions (e.g. Runge's function) for small  $N$ . For smooth functions like the harmonic example, a large value of  $d$  poses no problem and the rational interpolant offers spectral-like approximation and differentiation. Optimal selection of  $d$  and  $d_{\max}$  is problem dependent and an area of ongoing research [39, 43].

In contrast to the modal complex exponential basis set upon which the spectral vanishing viscosity is based, the nodal basis of the rational interpolant can not be decomposed into modal components to damp only the highest-frequencies. Instead, a dissipation operator derived from barycentric rational interpolants is employed at dynamically-blanked nodes. The dissipation operator is applied only at the two interval boundary nodes to avoid sacrificing accuracy within the interior of the temporal domain.

## IV. Implementation

The hybrid Time-Spectral scheme has been implemented within NASA's OVERFLOW code. OVERFLOW is an implicit, finite-difference-based Reynolds-averaged Navier-Stokes (RANS) solver developed to handle a wide range of flow calculations on overset grids[44]. To avoid solving the global implicit system at every iteration, OVERFLOW employs an approximate-factorization (AF) of the left-hand-side (LHS) of the discretized equations, whereby each dimension is solved sequentially. The AF scheme [45] solves a sequence of either block-tridiagonal or scalar-pentadiagonal systems, greatly reducing the computational effort required to update the solution at every iteration. The Time-Spectral scheme can be incorporated within this framework by adding an additional factor in the temporal dimension.

OVERFLOW solves the unsteady Navier-Stokes equations in strong conservation-law form.

$$\frac{\partial Q}{\partial t} + \frac{\partial F}{\partial x} + \frac{\partial G}{\partial y} = 0 \quad (22)$$

The flux vectors,  $F$  and  $G$ , in the  $x$ - and  $y$ -directions, respectively, are nonlinear functions of the state vector of conserved quantities,  $Q$ , that are comprised of both convective and viscous constituents. The equations are presented in Cartesian coordinates in two spatial dimensions but are solved in generalized curvilinear coordinates and implemented in three dimensions.

OVERFLOW is equipped with both steady-state and time-accurate modes but because only unsteady problems are considered, the time-accurate scheme will be briefly outlined and followed by a description of the Time-Spectral discretization and implementation.

### Time-Accurate Scheme

In the general case of time-dependent flow, a dual time-stepping scheme [46] is applied to sufficiently reduce the unsteady residual at each physical time step. The time-derivative of the state vector of conserved quantities is approximated with a second-order backward difference formula (BDF2).

$$\frac{3Q^{n+1} - 4Q^n + Q^{n-1}}{2\Delta t} + \delta_x F^{n+1} + \delta_y G^{n+1} = 0 \quad (23)$$

The spatial finite-difference operators,  $\delta_x$  and  $\delta_y$ , are applied to the corresponding flux vectors in the  $x$ - and  $y$ -directions, respectively. The dual-time advancement scheme is achieved by adding a pseudotime derivative approximated by the first-order backward Euler scheme, with subiteration index  $s$ .

$$\frac{Q^{s+1} - Q^s}{\Delta\tau} + \frac{3Q^{s+1} - 4Q^s + Q^{s-1}}{2\Delta t} + \delta_x F^{s+1} + \delta_y G^{s+1} = 0 \quad (24)$$

As the flux vectors are nonlinear functions in  $Q$ , they are linearized about  $Q^s$ . The linearizations are substituted into Eq. (24) which is then put into *delta* form, where  $A$  and  $B$  are the flux Jacobians in the  $x$ - and  $y$ -directions, respectively,  $\Delta\tilde{\tau} = \Delta\tau / (1 + \frac{3\Delta\tau}{2\Delta t})$  and  $\Delta Q = Q^{s+1} - Q^s$ .

$$\begin{aligned} & \left[ I + \Delta\tilde{\tau}\delta_x A + \Delta\tilde{\tau}\delta_y B \right] \Delta Q = \\ & -\Delta\tilde{\tau} \left[ \frac{3Q^s - 4Q^{s-1} + Q^{s-2}}{2\Delta t} + \delta_x F^s + \delta_y G^s \right] \end{aligned} \quad (25)$$

Approximately factoring the LHS of Eq. (25) results in the final form of the system of equations, where  $\mathbf{R}(Q^s)$  is the right-hand-side (RHS) of Eq. (25).

$$\left[ I + \Delta\tilde{\tau}\delta_x A \right] \left[ I + \Delta\tilde{\tau}\delta_y B \right] \Delta Q = \mathbf{R}(Q^s) \quad (26)$$

The solution is updated by applying a sequence of low-rank inversions onto the RHS of Eq. (26) on a point-by-point basis. This second-order accurate dual time-stepping procedure is used for the time-accurate calculations presented in §V.

### Time-Spectral Scheme

The Time-Spectral scheme is introduced as a modification to the discretization of the time-derivative in Eq. (23), where an infinitely-supported spectrally-accurate temporal differentiation operator replaces an algebraically-accurate finite-difference approximation.

$$\sum_{j=0}^{N-1} d_j^n Q^{j,s+1} + \delta_x F^{n,s+1} + \delta_y G^{n,s+1} = 0 \quad (27)$$

Equation (27) holds for all time samples,  $n \in \{0, \dots, N-1\}$ , and the solution array  $Q^{n,s}$  corresponds to the  $s$ th iteration of the  $n$ th time sample; the same notation holds for the flux vectors. As with the time-accurate case, a backward Euler pseudotime continuation augments Eq. (27).

$$\frac{Q^{n,s+1} - Q^{n,s}}{\Delta\tau} + \sum_{j=0}^{N-1} d_j^n Q^{j,s+1} + \delta_x F^{n,s+1} + \delta_y G^{n,s+1} = 0 \quad (28)$$

Linearizations of the flux vectors about  $Q^{n,s}$  are substituted into Eq. (28), which is then put into *delta* form where  $A$  and  $B$  are the same flux Jacobians as those first described for the Time-Accurate scheme.

$$\begin{aligned} & \frac{\Delta Q^n}{\Delta\tau} + \sum_{j=0}^{N-1} d_j^n \Delta Q^j + \left[ \delta_x A + \delta_y B \right] \Delta Q^n = \\ & - \left[ \sum_{j=0}^{N-1} d_j^n Q^{j,s} + \delta_x F^{n,s} + \delta_y G^{n,s} \right] \end{aligned} \quad (29)$$

We can express Eq. (29) over the complete space time domain where

$$\begin{aligned} \Delta \mathbf{Q} &= \{ \Delta Q^0, \dots, \Delta Q^{N-1} \} \\ \mathbf{R}(\mathbf{Q}) &= \{ \mathbf{R}(Q^0), \dots, \mathbf{R}(Q^{N-1}) \} \end{aligned}$$

are arrays of the update and spatial residual, respectively, over both space and time. The global temporal differentiation operator,  $D_N$ , is constructed via permutations of the local temporal differentiation operator,  $\mathcal{D}_N$  and  $\tilde{A}$  and  $\tilde{B}$  are block diagonal spatial Jacobian operators applied over all  $N$  time instances.

$$\left[ I + \Delta\tau D_N + \Delta\tau\delta_x \tilde{A} + \Delta\tau\delta_y \tilde{B} \right] \Delta \mathbf{Q} = \mathcal{R}(\mathbf{Q}^s), \quad (30)$$

where  $\mathcal{R}(\mathbf{Q}^s) = -\Delta\tau [D_N \mathbf{Q}^s + \mathbf{R}(\mathbf{Q}^s)]$ . Finally, the LHS of Eq. (30) is approximately-factored, treating time as an additional direction.

$$\left[ I + \Delta\tau\delta_x \tilde{A} \right] \left[ I + \Delta\tau\delta_y \tilde{B} \right] \left[ I + \Delta\tau D_N \right] \Delta \mathbf{Q} = \mathcal{R}(\mathbf{Q}^s) \quad (31)$$

The solution is updated by applying a sequence of  $N_{SD} + 1$  directional inversions onto the RHS of Eq. (31),  $\mathcal{R}(\mathbf{Q}^s)$ . The initial updates are performed in the  $N_{SD}$  spatial dimensions for each time sample  $j$  and the final inversion is performed in the temporal dimension at every point in space, indexed by  $i$ , using the dense local temporal differentiation operator.

$$\left[ I + \Delta\tau\delta_x A \right] \Delta \bar{Q}^j = \mathcal{R}(Q^{j,s}) \quad (32)$$

$$\left[ I + \Delta\tau\delta_y B \right] \Delta \bar{Q}^j = \Delta \bar{Q}^j \quad (33)$$

$$\left[ I + \Delta\tau \mathcal{D}_N \right] \Delta Q_i = \Delta \bar{Q}_i \quad (34)$$

The required modifications to the existing solver are limited to an additional linear solve, of at most dimension  $N$ , at every grid point for the Time-Spectral AF operator, and an evaluation of the temporal derivative at every grid point (a matrix-vector product of dimension  $N$ ). In other words, time is treated in a similar fashion to the spatial independent variables when solving for the steady-state solution in the combined space-time domain.

For spatial nodes with complete time histories, the standard Fourier-based differentiation operator is used for  $\mathcal{D}_N$ . However, for dynamically-blanked nodes,  $\mathcal{D}_N$  derived from a rational interpolant of dimension  $N_P < N$ , is dynamically generated and used for the intervals of  $N_P$  consecutively-defined time samples. For statically-blanked (Fourier-based) nodes, the approximately-factored Time-Spectral implicit temporal operator,  $[I + \Delta\tau \mathcal{D}_N]$ , can be diagonalized by the discrete Fourier transform if  $\Delta\tau$  is held constant for each time-sample ( $\Delta\tau$  is still free to change in space to enable local *pseudo* time stepping). Thus, the temporal update at statically-blanked nodes is reduced from an implicit linear system of equations to a series of scalar equations, removing the need for an inversion of the dense LHS operator. Replacing the direct linear solution with a fast Fourier transform (FFT) and inverse transform (IFFT) reduces the complexity from  $\mathcal{O}(N^3)$  to  $\mathcal{O}(N \log N)$  which matches that of the explicit NLF method [47].

$$\begin{aligned} \tilde{R} &\leftarrow \text{FFT}(\Delta \bar{Q}_i) \\ \Delta \tilde{Q}_k &\leftarrow \tilde{R}_k / (1 + \Delta\tau i\omega k), \quad \forall k \\ \Delta Q_i &\leftarrow \text{IFFT}(\Delta \tilde{Q}) \end{aligned}$$

Similarly, explicit evaluation of  $D_N \mathbf{Q}$  on the RHS can be evaluated by applying the FFT to  $\mathbf{Q}$ , differentiating in the frequency domain by multiplication of  $i\omega k$  and applying an IFFT to the differentiated data. If the time steps vary for each time-sample then the standard approach of performing a direct solve of  $[I + \Delta\tau \mathcal{D}_N]$  can still be used. This treatment is also required for dynamically-blanked nodes because there exists no similarity transform of the rational interpolant-based differentiation operator to the authors' knowledge.

The Time-Spectral approach as applied to OVERFLOW avoids modifying the existing spatial residual and implicit operators because they are applied to each time sample sequentially within each iteration. Second-order finite differences are used for all of the cases

presented, with second- and fourth-difference artificial dissipation using OVERFLOW's default settings of  $\epsilon_2 = 2.0$  and  $\epsilon_4 = 0.04$  dissipation coefficients. The primary convergence acceleration technique employed by OVERFLOW is the Full Approximation Storage (FAS) multigrid algorithm. It is desirable to include multigrid within the Time-Spectral implementation to make simulations of increasingly complex three-dimensional problems more tractable. The FAS *spatial* multigrid scheme was augmented to include the fully-implicit Time-Spectral scheme on all grid levels. The Time-Spectral multigrid implementation has demonstrated a multifold increase in computational efficiency [25].

Approximate-factorization schemes are prone to numerical instabilities in three or more dimensions. The three dimensional Time-Spectral AF scheme applies a sequence of four operators. Thomas et al. [11, 12] and Custer [13] demonstrate the stability of a two-factor Time-Spectral AF scheme. However, three- and four-factor periodic central-difference AF schemes are unconditionally unstable absent dissipation. Linear stability analysis in [25] demonstrates conditional stability for the Time-Spectral AF scheme in two and three spatial dimensions by applying artificial dissipation to the spatial operators alone. This treatment maintains the spectral accuracy of the non-dissipative temporal differentiation operator.

Naturally, there are both storage and computational overheads associated with a Time-Spectral calculation above the costs associated with an analogous steady-state computation. The extra cost is offset by the capability of converging to a space-time solution more rapidly than a time-accurate calculation. The efficiency merits of Fourier pseudospectral methods have been demonstrated in great detail by McMullen [4, 47] among others. Therefore, only the costs specific to the current implementation will be described.

Complete space-time solution and residual arrays must be stored for each of the  $N$  time samples. If  $N_x$  is the number of spatial nodes and  $N_Q$  is the number of solution variables, then the total memory for the global solution and residual arrays are each  $N \times (N_x \times N_Q)$ . Metric terms are also stored for each of the  $N$  time samples to avoid reevaluation at every iteration. The metric array is  $13N_x$  (in three dimensions), so an additional  $N$  copies are stored. An array storing a single integer blanking value at every spatial node is also required; if memory is limited then a low-storage option can be used where the metric and blanking arrays are reevaluated at every iteration. For example, a computation involving 125 million nodes distributed across fifty 20-core Ivy Bridge nodes, each equipped with 64GB of memory, can still employ upwards of one hundred time samples, which is beyond what is typically used in practice. While this suggests that a large number of temporal modes can be applied without risk of exhausting the memory budget on suitably parallelized calculations, there is also an opportunity to introduce a second level of parallelization by distributing the time samples onto different processors. This parallel-in-time Time-Spectral strategy was first demonstrated by Mavriplis and Yang [17].

The primary computational overhead resulting from the implicit approximately-factored Time-Spectral solver is attributed to the evaluation of the temporal derivative and the linear solve in the temporal dimension at every mesh point. Other processes require additional computation, such as loading and unloading data as the process loops through each time sample, but the impact should be minimal with proper implementation. As mentioned above, the  $\mathcal{O}(N \log N)$  FFT/IFFT can be used to reduce the computational cost of both the temporal derivative evaluation and the linear solve if constant time-stepping is used at a particular spatial node. Dynamically-blanked nodes cannot employ the FFT and therefore require a matrix-vector product and a linear solve, but the number of dynamically-blanked nodes is generally a small fraction of the overall number of spatial degrees of freedom. The matrix-vector product and linear solves can also be used for the Fourier-based nodes, but the savings afforded by the FFT become quite significant with even a modest number of temporal modes.

## V. Numerical Results

Numerical results obtained with the standard and Time-Spectral augmented OVERFLOW solvers applied to inviscid high-amplitude and laminar high-frequency oscillating airfoils are presented. However, computational efficiency of the Time-Spectral method is not explicitly addressed here. The literature provides strong support for Fourier collocation schemes due to their ability to compute periodic steady-state flows up to an order of magnitude more rapidly than traditional time-marching schemes. Instead, the primary objective of the numerical experiments is to demonstrate the ability of the standard and hybrid Time-Spectral schemes to produce results in agreement with the time-accurate solver. Well-resolved time-accurate calculations are taken as the reference solutions and are used to assess the accuracy of the Time-Spectral results.

The section begins with a subsonic inviscid plunging NACA 0012 airfoil test case. A large plunging amplitude results in a substantial number of dynamically-blanked nodes that are swept out by the airfoil over the course of the oscillation. Results using time-accurate, standard Time-Spectral (absent relative motion) and the hybrid Time-Spectral schemes are compared. Analysis of a pair of low-speed, high-frequency laminar plunging cases is used to investigate the dependence of temporal convergence of the Time-Spectral schemes on the fundamental frequency,  $\omega$ , of the oscillation and the need to damp aliasing errors for large  $\omega$ .

### Large-Amplitude Inviscid Plunging Airfoils

A large-amplitude inviscid plunging NACA 0012 airfoil test case provides a meaningful demonstration of the hybrid Time-Spectral scheme as it results in a significant number of dynamically-blanked nodes. This section first examines the accuracy of the schemes discussed in §III by evaluating how closely the Time-Spectral solution approximates the time-accurate solution at a dynamically-blanked sensor node. Modal convergence is then demonstrated for both the rigid- and relative-motion cases.

The instantaneous vertical displacement,  $y(t) = h \sin(kt)$ , is defined as a single sinusoid of the reduced frequency,  $k = \omega c / V_\infty$ . The plunging amplitude is selected as half the chord length, resulting in a nondimensional plunging amplitude,  $h = a/c = 0.5$ , with a reduced frequency of  $k = 0.1627$  radians per nondimensional time unit. A sensor node located on the Cartesian grid at the midchord position ( $x = 0.5c$ ) of the neutral axis of oscillation ( $y = 0$ ) experiences the maximum plunging velocity. The freestream Mach number is chosen as  $M_\infty = 0.5$  to maintain subsonic flow throughout the domain. A near-body O-mesh with  $241 \times 30$  points in the chordwise and body-normal directions, respectively, is embedded within a  $341 \times 261$  rectangular off-body grid that stretches approximately  $100c$  to the farfield boundaries in both the  $x$ - and  $y$ -directions. The hole cut is targeted at  $0.1c$  off the surface of the airfoil.

Figure 7 tracks the time history of streamwise momentum at the dynamically-blanked sensor node for several of the aforementioned candidate treatments, including barycentric rational interpolants, a least-squares Fourier projection and the spatial smoothing approach. Streamwise momentum,  $\rho u$ , is the most sensitive of the conserved quantities is therefore used to assess the performance of each scheme. The airfoil initially blanks the sensor node as it moves upwards and blanks it again as it makes its downward stroke. The node is blanked again as the airfoil completes its cycle. Accuracy is measured by computing the root-mean square (RMS) error of the Time-Spectral versus time-accurate solution at the unblanked collocation points. Solutions computed with the bounded interval approach using barycentric rational interpolants are shown in Fig. 7a and compared against the use of the globally expanded least-squares Fourier projection in Fig. 7b and the spatial smoothing approach in Fig. 7c. The three methods all perform similarly for the cases of three and five global collocation points, but the bounded interval approach demonstrates better agreement for the cases using additional global time samples. Even using  $N = 33$  global collocation points, both of the Fourier expansions exhibit high-frequency oscillations in the solution whereas the result computed using two independent partitioned segments spanned by barycentric rational interpolants demonstrates no such oscillations (in the scale of the figure). The superior convergence of the bounded interval approach

is confirmed in Fig. 7d where three choices of  $d_{\max}$  are presented for the barycentric rational interpolant in addition to the spatial smoothing approach and the global least-squares approach; a constant, zero-derivative result is plotted as a reference. While this analysis is presented for a single representative node, the results demonstrate the general behavior observed at all of the sensor nodes surveyed to date. For the remainder of the discussion, the default treatment for dynamically-blanked nodes is the barycentric rational interpolant using  $d_{\max} = 1$ .

The previous analysis examined the accuracy of the hybrid Time-Spectral approach at a particular dynamically-blanked grid point. However, design is often driven by functionals of integrated scalar performance measures such as lift and drag. Drag coefficient polars are therefore used to evaluate how well the Time-Spectral solutions match the time-accurate result. The Time-Spectral solutions are interpolated from their collocation points to reconstruct a continuous signal over the period. Continuous time histories of force and moment coefficients are then evaluated from these synthesized solutions and compared to the time-accurate solution.

Figure 8 plots the time-accurate sectional drag coefficient,  $c_d$ , versus vertical displacement,  $h$ , over the period against the Time-Spectral results for  $N \in \{3, 9, 33\}$ . The time-accurate calculation is initialized with a steady state solution and simulated for ten periods of motion. The drag signal settles into a periodic steady state relatively quickly. For the case of  $N = 3$ , depicted in Fig. 8a, neither the standard Time-Spectral method nor the hybrid Time-Spectral method accurately match the drag coefficient signal generated with the time-marching scheme. However, solution values at the collocation points strongly agree with the time-accurate result, especially for the rigid-motion case using the standard Time-Spectral method. As the temporal resolution is refined to  $N = 9$ , as depicted in Fig. 8b, both the rigid- and relative-motion interpolated signals demonstrate strong agreement with the time-accurate signal, although slight discrepancies between the standard and hybrid Time-Spectral methods remain. Finally, for the case of  $N = 33$ , depicted in Fig. 8c, the two Time-Spectral methods demonstrate complete agreement with each other and the time-accurate scheme.

Monotonic convergence of both the standard (Figure 9a) and hybrid (Figure 9b) Time-Spectral calculations are demonstrated in Fig. 9 by plotting the continuous drag coefficient signals for  $N \in \{3, 5, 9, 17, 33\}$  versus the periodic steady-state time-accurate signal. For the case of rigid motion using the standard Time-Spectral method, the signal computed using two harmonics ( $N = 5$ ) nearly matches the time-accurate result. However, the hybrid scheme for the relative motion case requires four to eight harmonics to achieve similar agreement with the time-accurate signal. Thus, the relative motion case requires additional modes beyond the number used for the rigid-motion case to achieve the same level of qualitative agreement with the time-accurate case.

This case has demonstrated the ability of the proposed hybrid Time-Spectral scheme to successfully predict the performance of a plunging airfoil that moves relative to a stationary background grid. However, the convergence of the relative-motion Time-Spectral scheme lags behind its rigid-motion counterpart. The sub-optimal basis functions used to describe the solution at dynamically-blanked nodes is partially responsible for this but so too is the fact that the stationary background grid is not moving with the body; the solution on the background grid remains periodic, however, its frequency content is augmented by the relative motion between itself and the plunging near-body grid. Consider the solution at a point on the near-body grid moving with the airfoil. Over the course of the period of motion, it experiences smooth transitions between compressions and expansions. While a stationary point on the background grid in the vicinity of the airfoil experiences periodic compressions and expansions, the transitions become more rapid as the plunging amplitude increases; the airfoil moves past the stationary point with a larger velocity and therefore the transition occurs over a shorter duration. This increases the frequency of the response that needs to be approximated by the discrete Fourier series. Therefore, for a given plunging amplitude and reduced frequency, more modes may need to be retained in order to resolve the relative-motion case because its solution contains higher-harmonics on the stationary grid.

Figures 10 and 11 provide the time- and frequency-response, respectively, of the subsonic inviscid plunging airfoil at a node located

approximately  $0.35c$  downstream of the trailing edge on both the near- and off-body grids in the neutral position of the oscillation ( $y = 0$ ). For the case of rigid-body motion, the off-body grid translates with the near-body grid and the nodes remain approximately coincident for all time. For the case of relative motion, the node on the off-body grid remains in place and is therefore only approximately coincident with the node on the near-body grid at two times over the period of oscillation. The higher-frequency content in the solution at a node on the stationary background grid suggests that more frequencies are required to resolve the solution using relative motion than with rigid motion. This assertion is supported by Fig. 12 that plots the reconstruction of the off-body grid solution from the frequency components defined by a discrete Fourier transform of the time-accurate solution. Figure 12a demonstrates that roughly four modes are sufficient to adequately resolve the solution at the off-body grid point for the case of rigid-body motion. However, the reconstructions plotted in Fig. 12b suggest that thirty or more modes are required to sufficiently resolve the flow at the stationary off-body grid point. However, many fewer modes are required to match the time-accurate result with respect to integrated loads such as drag (Figure 9), supporting the Time-Spectral method as a potential reduced-order model (ROM). For such simple cases, rigid motion would naturally be a more efficient choice as fewer modes are required to resolve the flow. However, more complex configurations require relative motion for non-deforming grids.

### High-Frequency Laminar Plunging Airfoils

Low speed, low Reynolds number laminar plunging NACA 0012 airfoil cases are investigated over a range of frequencies. Jones et al. [48] published results from low-speed experiments that serve to highlight the complex nature of the vortical structures associated with these flows as a function of their Strouhal number,  $St = kh$ , which is a product of their reduced frequency and nondimensionalized plunging amplitude. The instantaneous vertical displacement,  $y(t) = h \sin(kt)$ , is defined as a single sinusoid of the reduced frequency.

At low Strouhal numbers, the plunging motion produces a vortical wake with a momentum deficit, resulting in a time-averaged drag on the airfoil. As the frequency is increased, the vortical structure transforms, eventually resulting in a thrust-producing momentum surplus. Increasing the Strouhal number even further results in both lift and thrust. This behavior has been coined the *Knoller-Betz effect* after the experimentalists who first independently documented the phenomenon [48].

Two primary cases are investigated: a drag-producing case with  $St = 0.288$  and a higher-frequency, thrust-producing case with  $St = 0.6$ . The same freestream Mach number,  $M_\infty = 0.2$ , and Reynolds number,  $Re = 1850$ , are used for both cases. Each case is computed using both rigid- and relative-body motion to compare the performance between the standard and hybrid Time-Spectral methods.

#### Drag-Producing Case

The lower-frequency test case of  $St = 0.288$  with reduced frequency  $k = 3.6$  and plunging amplitude  $h = 0.08$  results in a vortical wake structure with a momentum deficit, producing a time-averaged drag on the airfoil. The case was simulated using time-accurate and Time-Spectral approaches for both rigid and relative motion and qualitatively compared to the experimental results offered in [48]. Figure 13 provides snapshots of the experimental flowfield and vorticity magnitude of the simulations. The time-accurate calculation successfully captures the primary flow features depicted in the experimental snapshot and the Time-Spectral simulations for both rigid and relative motion converge to a similar solution, provided sufficient temporal resolution of around 16 modes (Figures 13i and 13j) is used. There exist significant variations for the under-resolved Time-Spectral solutions between the rigid- and relative-motion cases, but the underlying wake structure is apparent with just one (Figure 13b) or two (Figure 13d) modes for the relative-motion case and just two (Figure 13c) or four (Figure 13e) modes for the rigid-motion case.

Figure 14 demonstrates the rapid convergence of the Time-Spectral computed sectional drag coefficient,  $c_d$ , to the time-accurate result. Employing just four modes (See Figure 14b) for either Time-Spectral configuration nearly matches the time-accurate signal. Thus, the scalar

performance measure of drag converges more rapidly than the qualitative vortical flow features.

### Thrust-Producing Case

As the Strouhal number is increased to  $St = 0.6$ , the vortical wake structure evolves from producing a momentum deficit, as demonstrated for  $St = 0.288$ , to a momentum surplus, where the time-averaged flow exhibits a thrust-inducing jet structure. Selecting a reduced frequency,  $k = 6.0$  and plunging amplitude  $h = 0.1$ , results in the particular wake structure depicted in Fig. 15. Experimental results taken from [48] and depicted in Fig. 15k use this Strouhal number,  $St = 0.6$ , except that the reduced frequency is halved and the plunging amplitude doubled ( $k = 3.0$  and  $h = 0.2$ ). Simulations using these parameters resulted in significantly different vortical wake patterns. Therefore, the case using the higher reduced frequency is employed, which is consistent with the observations and calculations by Allaneau and Jameson [49]. Figure 15 demonstrates strong agreement between the time-accurate and experimental data and again demonstrates the convergence of the Time-Spectral solutions for both rigid and relative motion with increased temporal resolution. As with the drag-producing cases, the Time-Spectral calculations require sixteen modes (Figures 15i and 15j) to qualitatively match the time-accurate solution. The bulk features of the wake are resolved using half as many modes, but the solutions do not match in the vicinity of the trailing edge. Figure 16 confirms the convergence of the Time-Spectral computed drag coefficient,  $c_d$ , to the time-accurate result for the thrust-producing case.

Unlike the drag-producing case using  $k = 0.288$ , spectral vanishing viscosity is required to enable adequately converge the Time-Spectral simulations for the thrust-producing configuration for both the rigid- and relative-body motion calculations. Initially, spectral vanishing viscosity is only applied to the statically-blanked (Fourier-based) nodes in the case of relative motion, leaving the dynamically-blanked nodes free of any added dissipation. For the relative motion case using eight harmonics ( $N = 17$ ), additional dissipation is required at the undamped, dynamically-blanked nodes as described in §IV.

## VI. Conclusions

A hybrid Time-Spectral method was developed to facilitate its use within an overset framework and its implementation within NASA's implicit OVERFLOW solver was outlined. The Time-Spectral augmented OVERFLOW solver was applied to inviscid high-amplitude and laminar high-frequency plunging airfoils cases. The high-amplitude plunging case demonstrated the superior performance of the bounded interval approach using barycentric rational interpolants, in particular, to represent the aperiodic temporal variation on equispaced nodes for such dynamically-blanked nodes. It was also shown that the use of relative motion requires additional resolution in contrast to using rigid motion, as a consequence of the added frequency content induced by the motion. Investigation of low-speed, laminar plunging airfoils demonstrated the ability of the standard and hybrid Time-Spectral schemes to accurately simulate solutions with highly-vortical wakes over a range of reduced frequencies and the need for temporal damping of particular high-frequency cases to facilitate adequate convergence for both the standard and hybrid Time-Spectral methods.

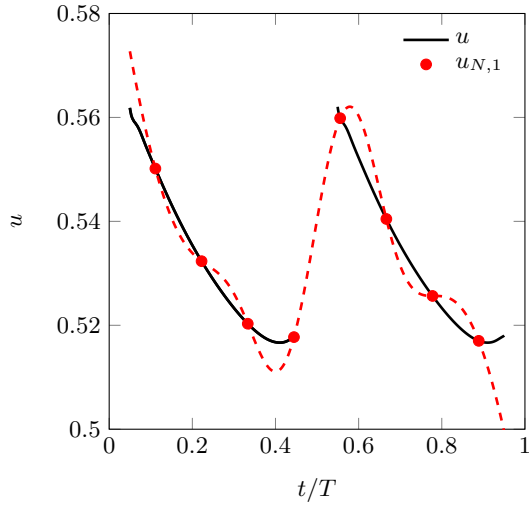
## Acknowledgments

The authors would like to thank the US Army Aviation Development Directorate (AMRDEC) for sponsoring this research and NASA Advanced Supercomputing (NAS) for providing the computational resources.

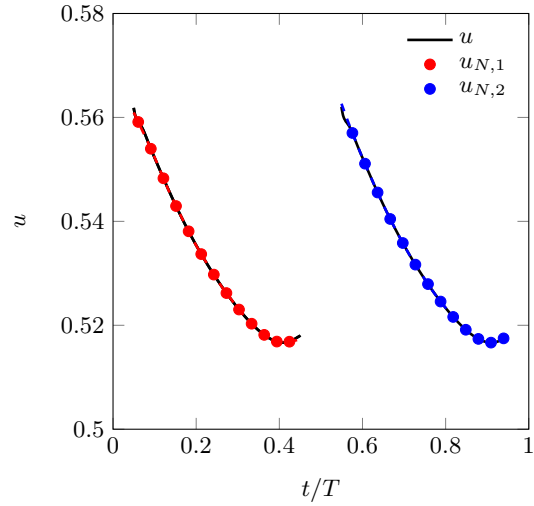
## References

- [1] Hall, K., Thomas, J., and Clark, W., "Computation of Unsteady Nonlinear Flows in Cascades using a Harmonic Balance Technique," *9th International Symposium on Unsteady Aerodynamics, Aeroacoustics and Aeroelasticity of Turbomachines*, Lyon, France, September 2000.
- [2] Hall, K. C., Thomas, J. P., and Clark, W., "Computation of Unsteady Nonlinear Flows in Cascades Using a Harmonic Balance Technique," *AIAA Journal*, Vol. 40, May 2002, pp. 879–886.
- [3] McMullen, M. and Jameson, A., "The computational efficiency of nonlinear frequency domain methods," *Journal of Computational Physics*, Vol. 212, 2006, pp. 637–661.
- [4] McMullen, M., Jameson, A., and Alonso, J., "Demonstration of Nonlinear Frequency Domain Methods," *AIAA Journal*, Vol. 44, No. 7, July 2006, pp. 1428–1435.
- [5] Nadarajah, S. K., McMullen, M. S., and Jameson, A., "Optimum Shape Design for Unsteady Flows Using Time Accurate and Non-Linear Frequency Domain Methods," AIAA Paper 3875, Orlando, Florida, June 2003.
- [6] Murman, S. M., "Reduced-Frequency Approach for Calculating Dynamic Derivatives," *AIAA Journal*, Vol. 45, No. 6, June 2007, pp. 1161–1168.
- [7] Gopinath, A. K. and Jameson, A., "Time Spectral Method for Periodic Unsteady Computations over Two- and Three-Dimensional Bodies," AIAA Paper 1220, Reno, Nevada, January 2005.
- [8] Gopinath, A. K. and Jameson, A., "Application of the Time Spectral Method to Periodic Unsteady Vortex Shedding," AIAA Paper 0449, January 2006.
- [9] Blanc, F., Roux, F.-X., Jouhaud, J.-C., and Boussuge, J.-F., "Numerical Methods for Control Surfaces Aerodynamics with Flexibility Effects," IFASD 2009, Seattle, WA, June 2009.
- [10] Canuto, C., Hussaini, M., Quarteroni, A., and Zang, T., *Spectral Methods: Fundamentals in Single Domains*, Scientific Computation, Springer, Berlin, 2006.
- [11] Thomas, J. P., Custer, C. H., Dowell, E. H., and Hall, K. C., "Unsteady Flow Computation Using a Harmonic Balance Approach Implemented about the OVERFLOW 2 Flow Solver," AIAA Paper 4270, San Antonio, Texas, June 2009.
- [12] Thomas, J. P., Custer, C. H., Dowell, E. H., Hall, K. C., and Corre, C., "Compact Implementation Strategy for a Harmonic Balance Method Within Implicit Flow Solvers," *AIAA Journal*, Vol. 51, No. 6, June 2013, pp. 1374–1381.
- [13] Custer, C. H., *A Nonlinear Harmonic Balance Solver for an Implicit CFD Code: OVERFLOW 2*, Ph.D. thesis, Duke University, 2009.
- [14] Soucy, O. and Nadarajah, S. K., "A NLF method for the simulation of periodic unsteady flows for overset meshes," AIAA Paper 4271, San Antonio, Texas, June 2009.
- [15] Mavriplis, D. J., Yang, Z., and Mundis, N., "Extensions of Time Spectral Methods for Practical Rotorcraft Problems," AIAA Paper 0423, Nashville, Tennessee, January 2012.
- [16] Choi, S., Potsdam, M., Lee, K., Iaccarino, G., and Alonso, J. J., "Helicopter Rotor Design Using a Time-Spectral and Adjoint-Based Method," AIAA Paper 5810, Victoria, British Columbia, September 2008.
- [17] Mavriplis, D. J. and Yang, Z., "Time Spectral Method for Periodic and Quasi-Periodic Unsteady Computations on Unstructured Meshes," AIAA Paper 5034, Chicago, Illinois, June 2010.
- [18] Peyret, R., *Spectral Methods for Incompressible Viscous Flow*, Applied Mathematical Sciences, Springer, New York, 2002.
- [19] Hesthaven, J. S., Gottlieb, S., and Gottlieb, D., *Spectral Methods for Time-Dependent Problems*, Cambridge Monographs on Applied and Computational Mathematics, Cambridge University Press, Cambridge, 2007.
- [20] Snider, A. D., "An Improved Estimate of the Accuracy of Trigonometric Interpolation," *SIAM Journal of Numerical Analysis*, Vol. 9, No. 3, September 1972, pp. 505–508.
- [21] Tadmor, E., "Convergence of Spectral Methods for Nonlinear Conservation Laws," *SIAM Journal of Numerical Analysis*, Vol. 26, No. 1, February 1989, pp. 30–44.
- [22] Maday, Y. and Tadmor, E., "Analysis of the Spectral Vanishing Viscosity Method for Periodic Conservation Laws," *SIAM Journal of Numerical Analysis*, Vol. 26, No. 4, August 1989, pp. 854–870.
- [23] Benek, J. A., Steger, J. L., and Dougherty, F. C., "A Flexible Grid Embedding Technique with Application to the Euler Equations," AIAA-83-1944-CP, 1983.

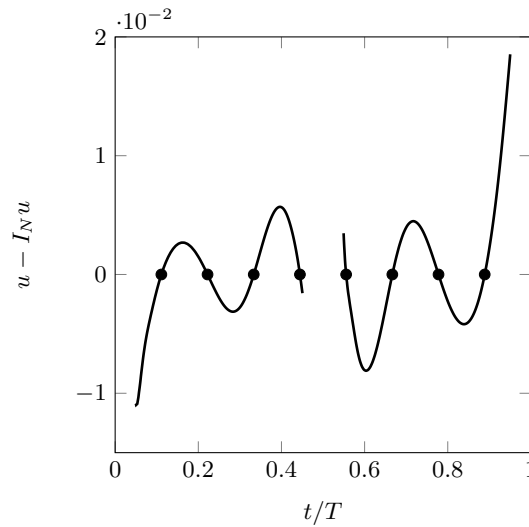
- [24] Leffell, J. I., Murman, S. M., and Pulliam, T. H., "An Extension of the Time-Spectral Method to Overset Solvers," AIAA Paper 0637, Grapevine, Texas, January 2013.
- [25] Leffell, J., *An Overset Time-Spectral Method for Relative Motion*, Ph.D. thesis, Stanford University, June 2014.
- [26] Maple, R. C., King, P. I., and Oxley, M. E., "Adaptive Harmonic Balance Solutions to Euler's Equation," *AIAA Journal*, Vol. 41, No. 9, September 2003, pp. 1705–1714.
- [27] Mosahebi, A. and Nadarajah, S., "An adaptive Non-Linear Frequency Domain method for viscous flows," *Computers & Fluids*, Vol. 75, 2013, pp. 140–154.
- [28] Strang, G., "The Optimal Coefficients in Daubechies Wavelets," *Physica D*, Vol. 60, 1992, pp. 239–244.
- [29] Romine, C. H. and Peyton, B. W., "Computing Connection Coefficients of Compactly Supported Wavelets on Bounded Intervals," Mathematical Sciences Section ORNL/TM-13413, Oak Ridge National Laboratory, April 1997.
- [30] Huybrechs, D., "On the Fourier Extension of Nonperiodic Functions," *SIAM Journal of Numerical Analysis*, Vol. 47, No. 6, 2010, pp. 4326–4355.
- [31] Boyd, J. P., "A Comparison of Numerical Algorithms for Fourier Extension of the First, Second, and Third Kinds," *Journal of Computational Physics*, Vol. 178, 2002, pp. 118–160.
- [32] Bruno, O. P., Han, Y., and Pohlman, M. M., "Accurate, high-order representation of complex three-dimensional surfaces via Fourier continuation analysis," *Journal of Computational Physics*, Vol. 227, 2007, pp. 1094–1125.
- [33] Candès, E., "Compressive sampling," International Congress of Mathematicians, Madrid, Spain, 2006.
- [34] Boyd, J. P., *Chebyshev and Fourier Spectral Methods*, Dover, Mineola, New York, Second (revised) ed., 2001.
- [35] Platte, R. B., Trefethen, L. N., and Kuijlaars, A. B., "Impossibility of Fast Stable Approximation of Analytic Functions from Equispaced Samples," *SIAM Review*, Vol. 53, No. 2, 2011, pp. 308–318.
- [36] Bos, L., De Marchi, S., Hormann, K., and Klein, G., "On the Lebesgue constant of barycentric rational interpolation at equidistant nodes," *Numerische Mathematik*, Vol. 121, No. 3, 2012, pp. 461–471.
- [37] Baltensperger, R. and Berrut, J.-P., "The linear rational collocation method," *Journal of Computational and Applied Mathematics*, Vol. 134, 2001, pp. 243–258.
- [38] Berrut, J.-P. and Baltensperger, R., "The Linear Rational Pseudospectral Method for Boundary Value Problems," *BIT*, Vol. 41, No. 5, 2001, pp. 868–879.
- [39] Klein, G., "An Extension of the Floater-Hormann Family of Barycentric Rational Interpolants," *Mathematics of Computation*, Vol. 82, No. 284, October 2013, pp. 2273–2292.
- [40] Tee, T. W. and Trefethen, L. N., "A Rational Spectral Collocation Method with Adaptively Transformed Chebyshev Grid Points," *SIAM Journal of Scientific Computing*, Vol. 28, No. 5, 2006, pp. 1798–1811.
- [41] Baltensperger, R., Berrut, J.-P., and Noël, B., "Exponential Convergence of a Linear Rational Interpolant Between Transformed Chebyshev Points," *Mathematics of Computation*, Vol. 68, No. 227, February 1999, pp. 1109–1120.
- [42] Floater, M. S. and Hormann, K., "Barycentric rational interpolation with no poles and high rates of approximation," *Numerische Mathematik*, Vol. 107, No. 2, August 2007, pp. 315–331.
- [43] Wang, Q., Moin, P., and Iaccarino, G., "A Rational Interpolation Scheme with Superpolynomial Rate of Convergence," *SIAM Journal of Numerical Analysis*, Vol. 47, No. 6, 2010, pp. 4073–4097.
- [44] Nichols, R., Tramel, R., and Buning, P., "Solver and Turbulence Model Upgrades to OVERFLOW 2 for Unsteady and High-Speed Applications," AIAA Paper 2824, San Francisco, CA, June 2006.
- [45] Beam, R. M. and Warming, R., "An Implicit Finite-Difference Algorithm for Hyperbolic Systems in Conservation-Law Form," *Journal of Computational Physics*, Vol. 22, 1976, pp. 87–110.
- [46] Jameson, A., "Time Dependent Calculations Using Multigrid, with Applications to Unsteady Flows Past Airfoils and Wings," AIAA Paper 1596, Honolulu, Hawaii, June 1991.
- [47] McMullen, M. S., *The Application of Non-Linear Frequency Domain Methods to the Euler and Navier-Stokes Equations*, Ph.D. thesis, Stanford University, Stanford, CA, March 2003.
- [48] Jones, K. D., Dohring, C. M., and Platzer, M. F., "Experimental and Computational Investigation of the Knoller-Betz Effect," *AIAA Journal*, Vol. 36, No. 7, July 1998, pp. 1240–1246.
- [49] Allaneau, Y. and Jameson, A., "Direct Numerical Simulations of Plunging Airfoils," AIAA Paper 0728, Orlando, Florida, January 2010.



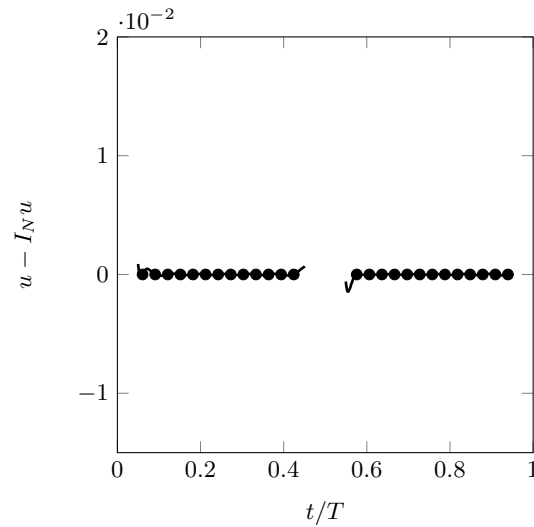
(a) Interpolated solution for 8 of 9 unblanked nodes through a single interval



(b) Interpolated solution for 26 of 33 unblanked nodes through two independent intervals



(c) Residual for 8 of 9 unblanked nodes within a single interval



(d) Residual for 26 of 33 unblanked nodes within two independent intervals

Figure 4: Barycentric rational interpolation and residual,  $e = u - I_N u$ , for  $N = 9$  and  $N = 33$  global collocation points with the default setting of  $d_{\max} = 1$ .

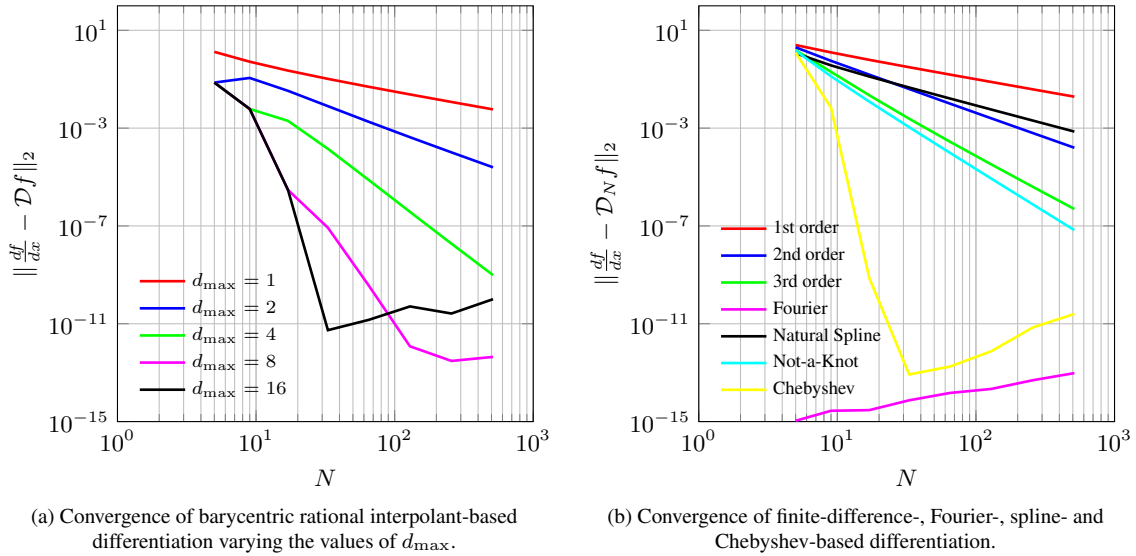


Figure 5: Convergence of differentiated harmonic function,  $f(x) = 1 + \cos(\pi x) + \sin(\pi x)$ ,  $x \in [-1, 1]$ , using the barycentric rational interpolant-based differentiation operator for different values of  $d_{\max}$  and other differentiation operators on equispaced nodes (Chebyshev on clustered Chebyshev nodes).

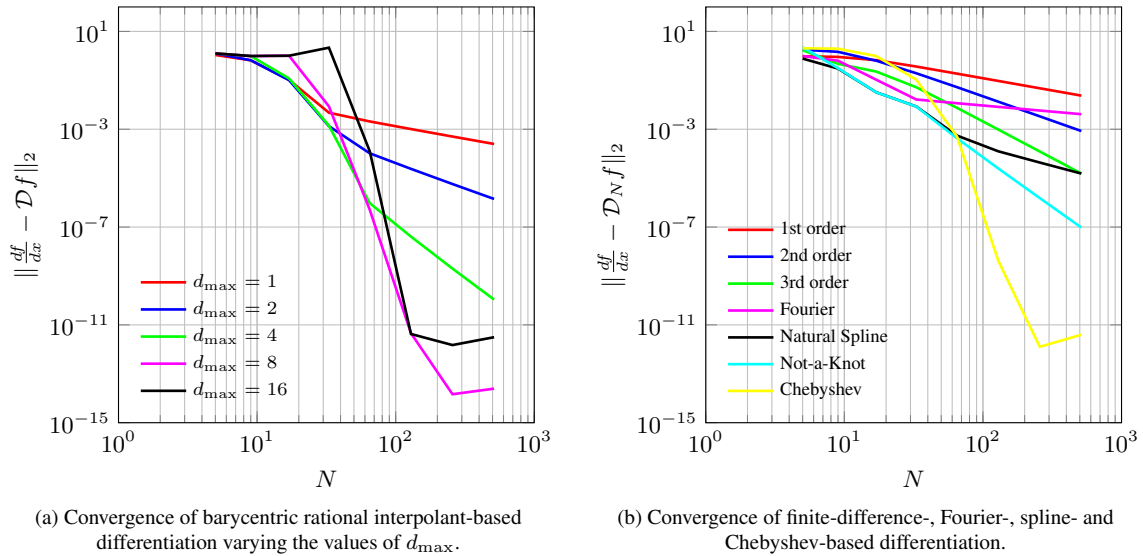


Figure 6: Convergence of differentiated Runge's function,  $f(x) = \frac{1}{1+25x^2}$ ,  $x \in [-1, 1]$ , using the barycentric rational interpolant-based differentiation operator for different values of  $d_{\max}$  and other differentiation operators on equispaced nodes (Chebyshev on clustered Chebyshev nodes).

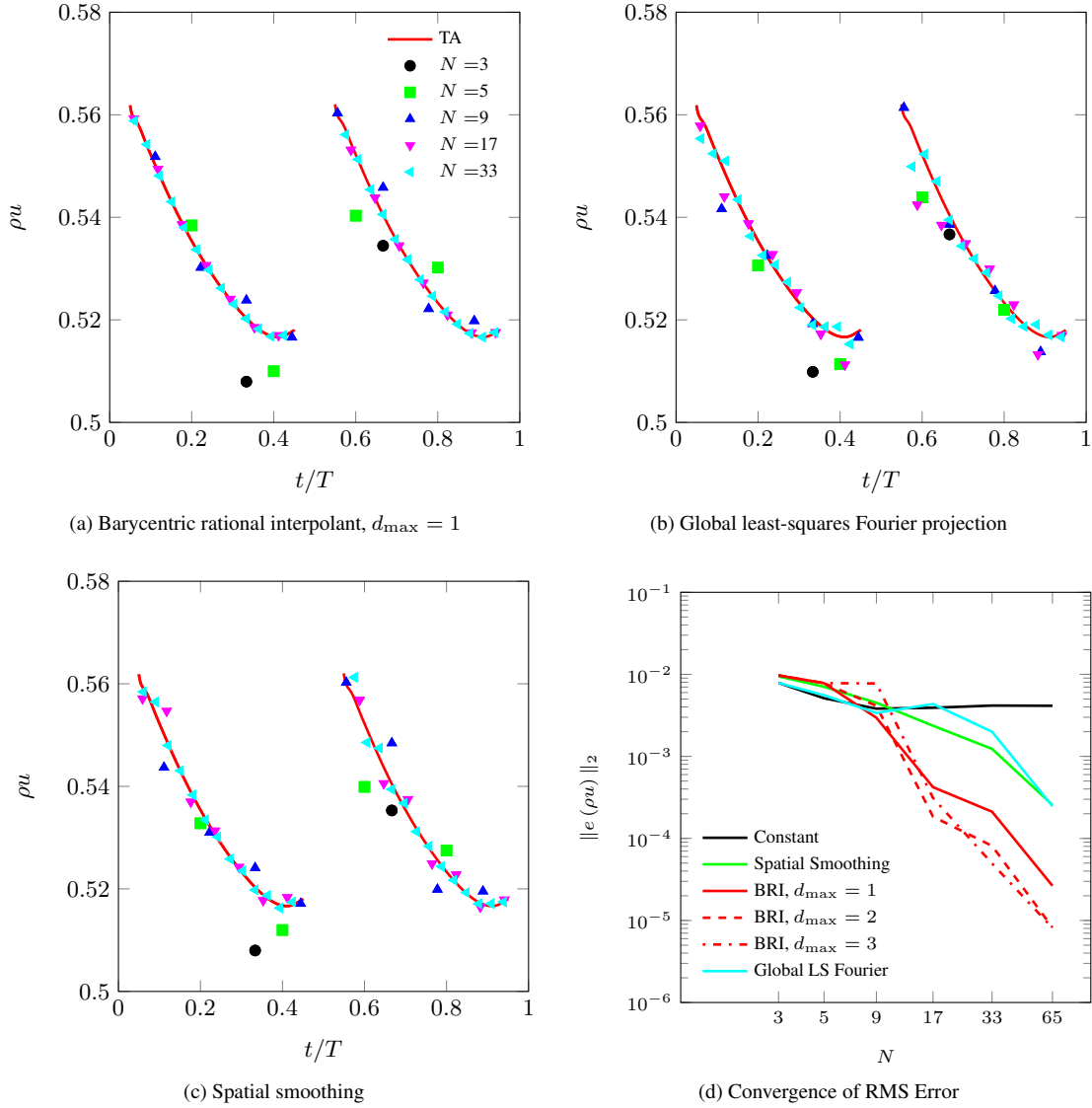


Figure 7: Inviscid Plunging Airfoil. Time-Spectral versus time-accurate values of streamwise momentum,  $\rho u$ , at sensor node using (a) barycentric rational interpolants with  $d_{\max} = 1$ , (b) a global least-squares Fourier projection and (c) spatial smoothing to treat dynamically-blanked nodes. Convergence of the RMS error of streamwise momentum of various hybrid Time-Spectral schemes versus the time-accurate solution at the sensor node is depicted in (d).

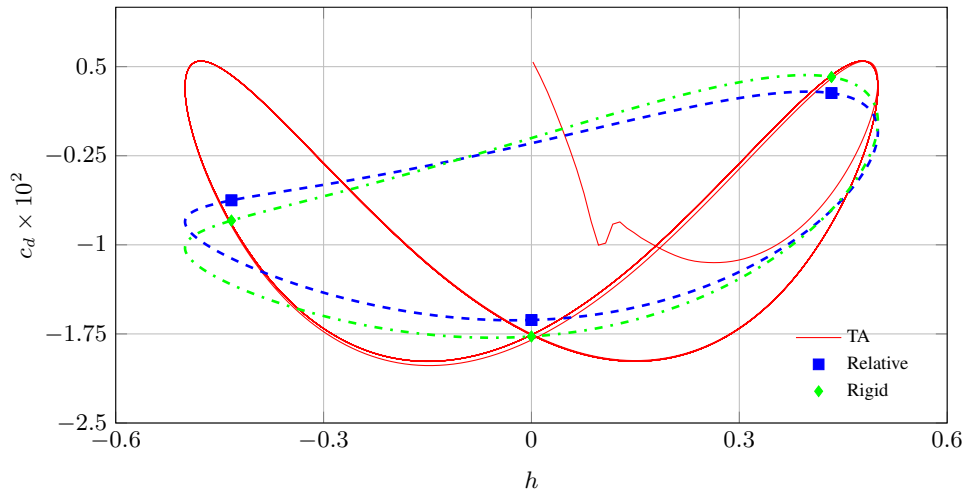
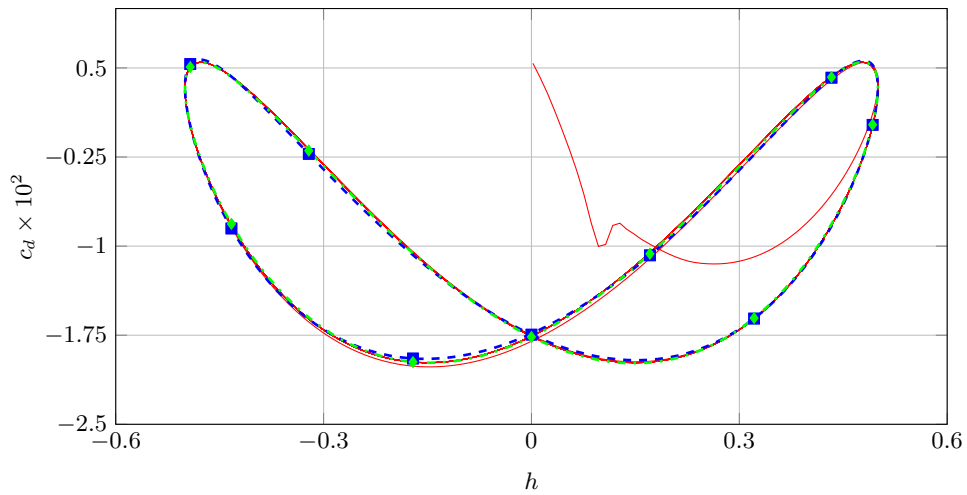
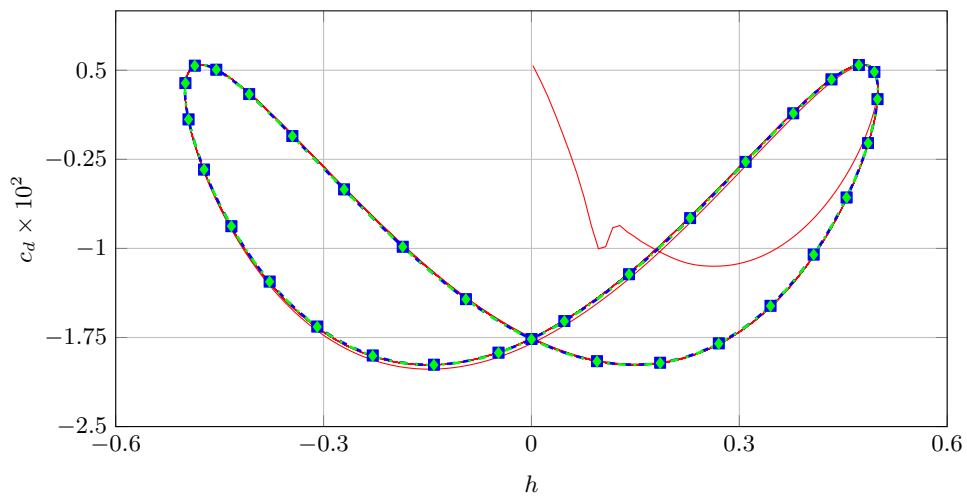
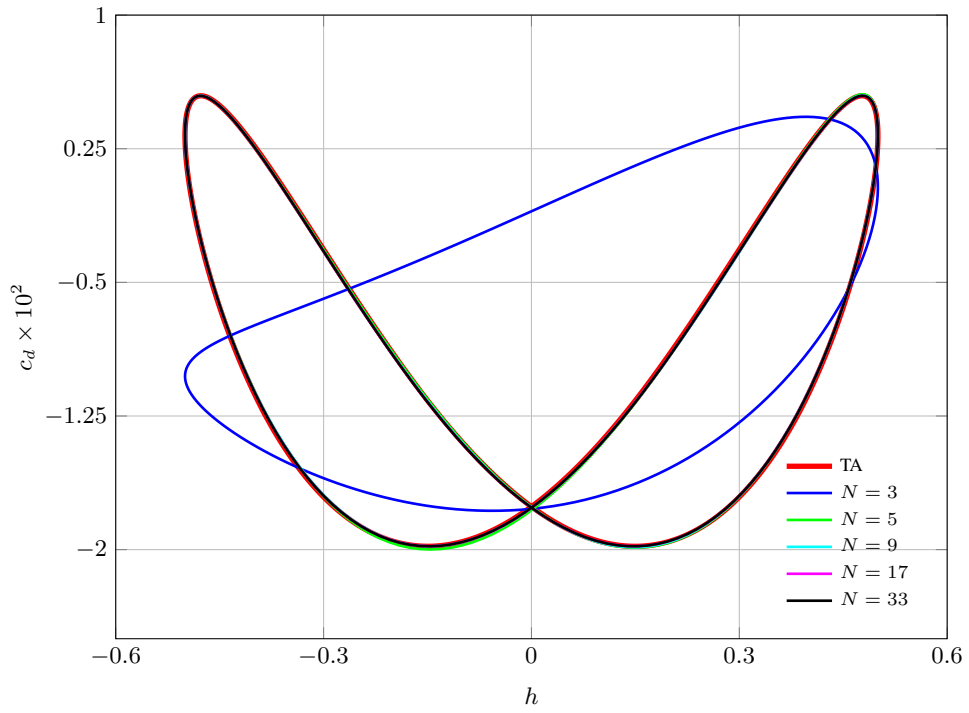
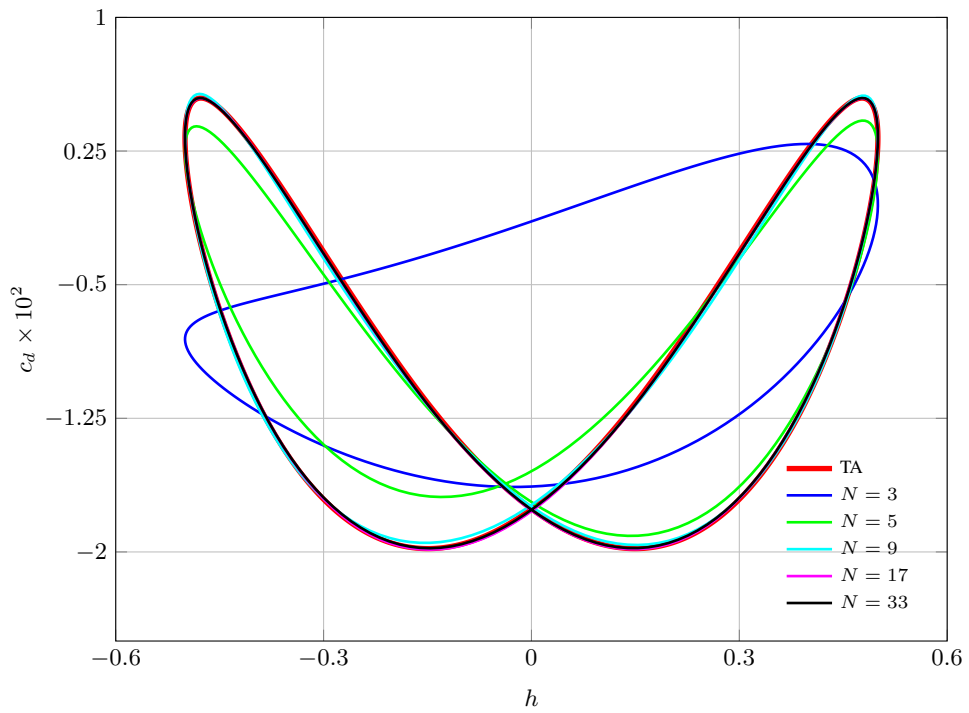
(a)  $N = 3$ (b)  $N = 9$ (c)  $N = 33$ 

Figure 8: Inviscid Plunging Airfoil. Time-Spectral versus time-accurate drag coefficients for  $N \in \{3, 9, 33\}$ . The time-accurate solution is plotted in red from steady-state startup. Blue squares and green diamonds locate the drag coefficient values at the Time-Spectral collocation points for relative- and rigid-body motion, respectively. Drag coefficient signals evaluated from reconstructed Time-Spectral solutions are plotted with hashed lines.



(a) Rigid Motion



(b) Relative Motion

Figure 9: Inviscid Plunging Airfoil. Convergence of (a) rigid- and (b) relative-motion Time-Spectral drag coefficient signals to the periodic steady-state time-accurate calculation for  $N \in \{3, 5, 9, 17, 33\}$ .

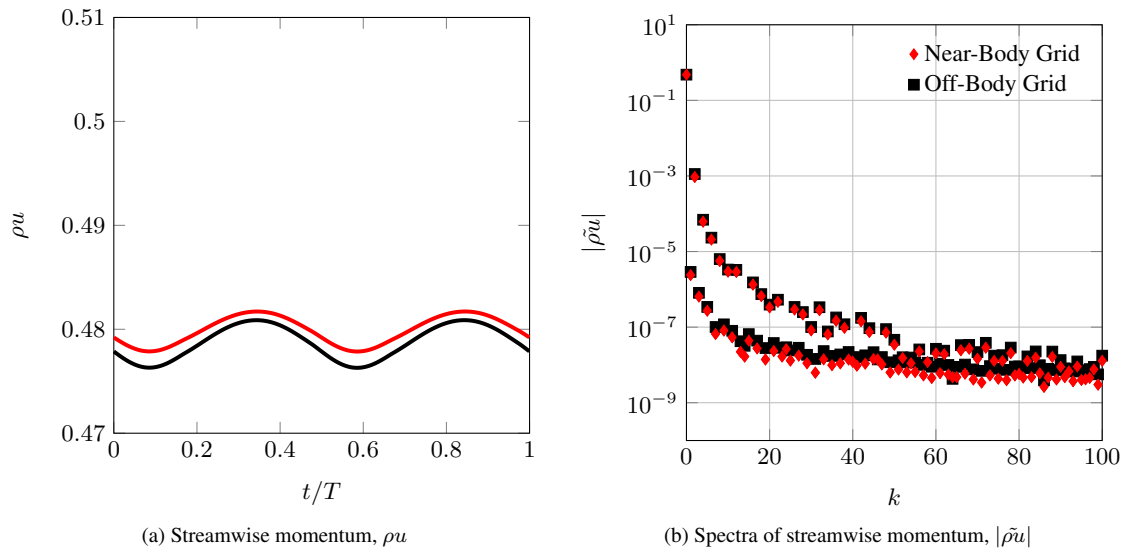


Figure 10: Inviscid Plunging Airfoil. Rigid motion case. Time and frequency response of a plunging airfoil with an off-body grid translating with the airfoil. The frequency components at the near- and off-body nodes are essentially identical.

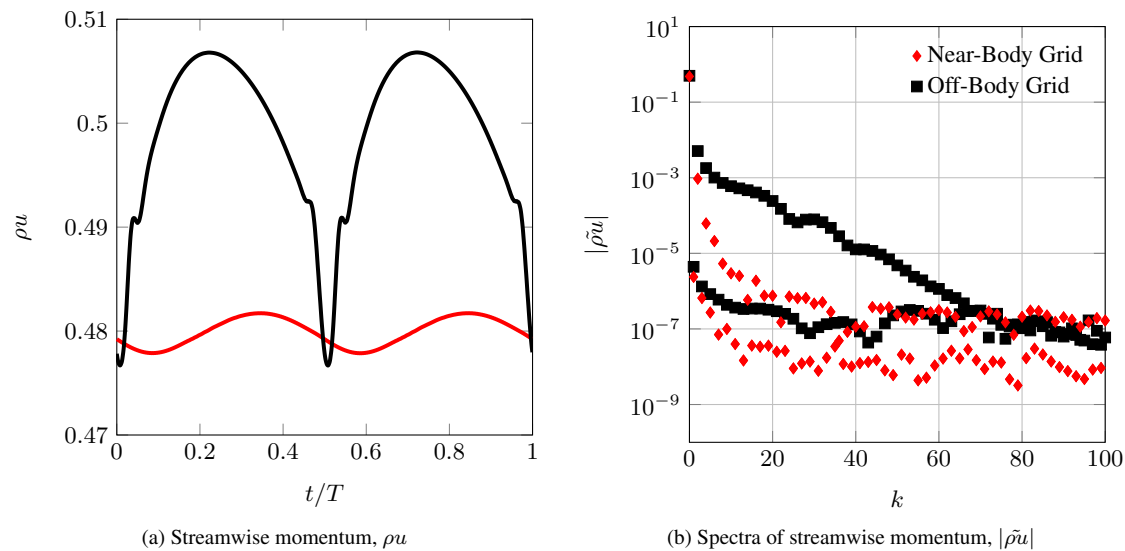
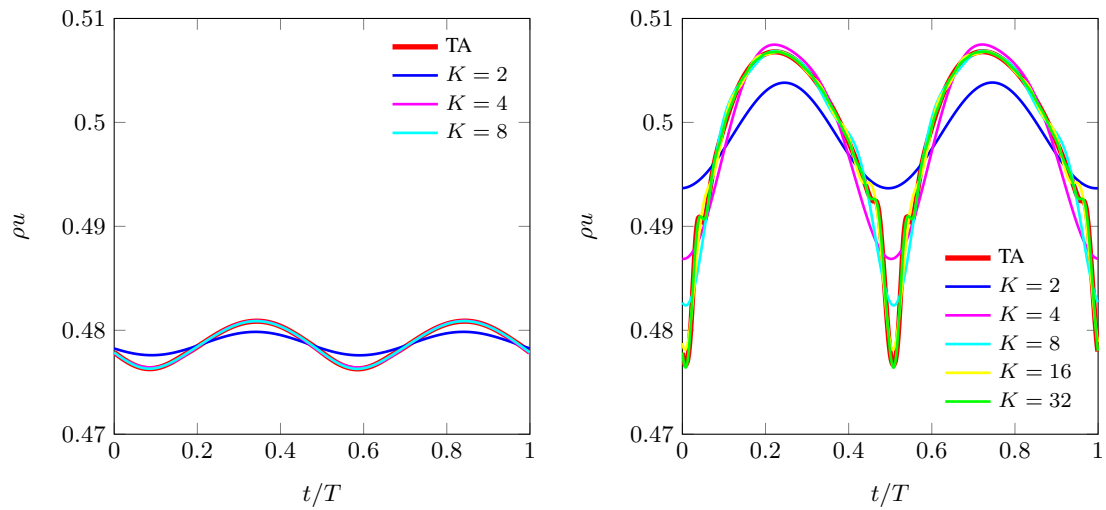


Figure 11: Inviscid Plunging Airfoil. Relative motion case. Time and frequency response of a plunging airfoil with a stationary background grid. The frequency components at the near- and off-body nodes are strikingly different with many more modes required to resolve the solution at the node on the stationary background grid. The node on the background grid is the same one described in Fig. 10a, but the background grid was translating with the airfoil in that case.



(a) Translating node on background grid for rigid-body motion. (b) Stationary node on background grid for relative-body motion.

Figure 12: Inviscid Plunging Airfoil. Reconstruction of streamwise momentum at a node on the off-body grid (a) translating with the airfoil and (b) stationary relative to the translating airfoil. The solution at the stationary node requires approximately  $K = 32$  modes to reasonably reconstruct the continuous signal whereas the solution at the translating node requires approximately  $K = 4$  modes. This suggests an inherent inefficiency of employing relative motion. However, rigid-body motion is not universally applicable and therefore relative-body motion must be used for certain configurations.

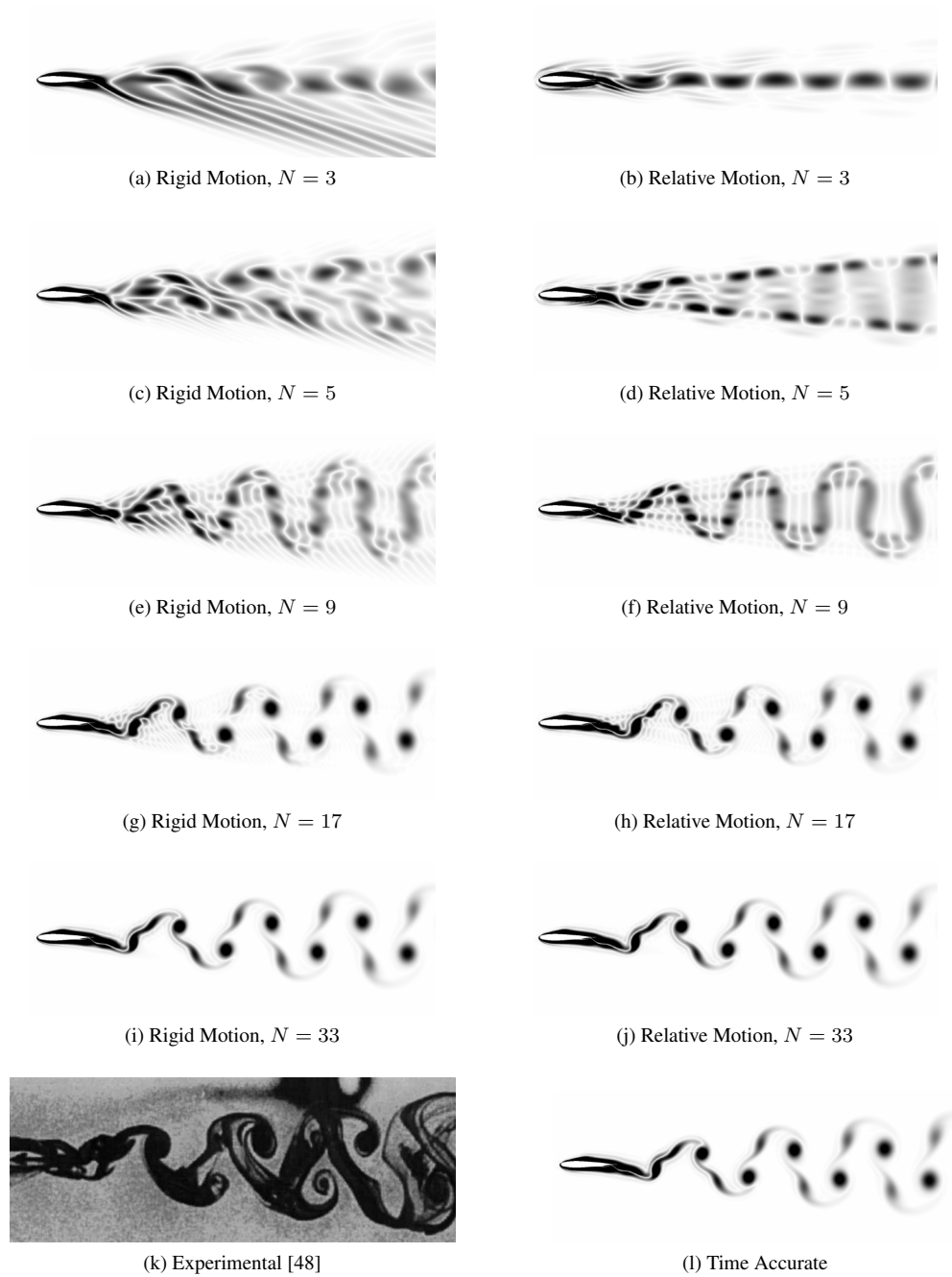


Figure 13: Laminar Plunging NACA 0012 Airfoil. Drag-producing case at  $M_\infty = 0.2$  and  $Re = 1850$ . Visualization of vorticity magnitude. Comparison of experimental with computed time-accurate and Time-Spectral results using  $N \in \{3, 5, 9, 17, 33\}$  for both rigid- and relative-body motion. Note that while certain flow features are not resolved by the lower-mode Time-Spectral cases, Fig. 14 suggests that using  $N \geq 9$  matches the time-accurate drag-coefficient for nearly the entire period of oscillation. Vorticity magnitude varies from 0 in white to greater than or equal to 1 in black.

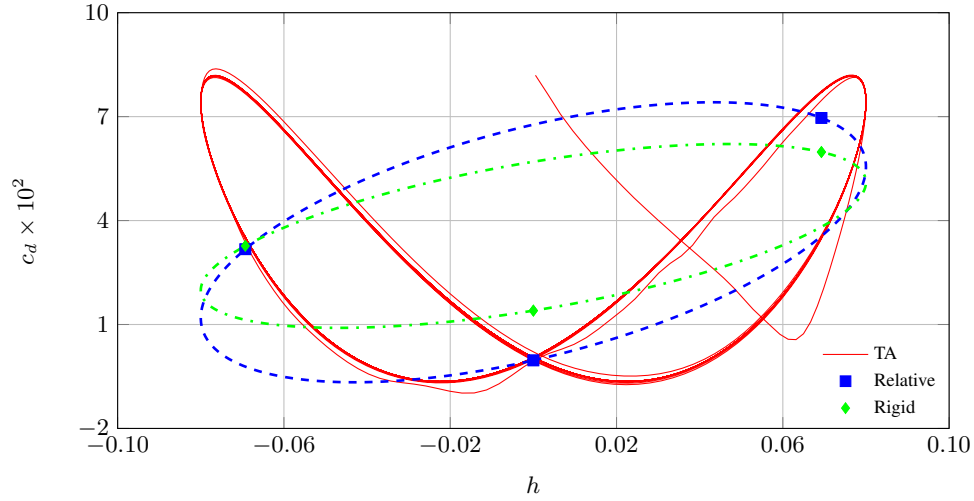
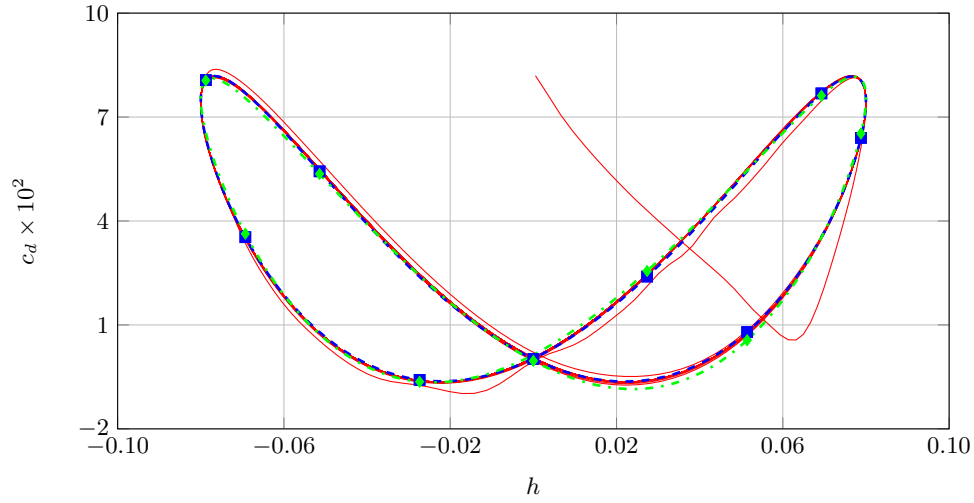
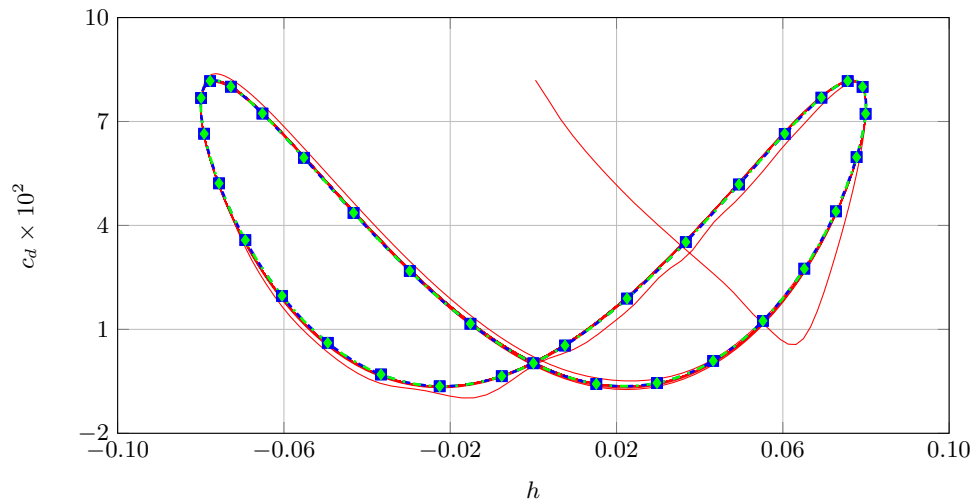
(a)  $N = 3$ (b)  $N = 9$ (c)  $N = 33$ 

Figure 14: Laminar Plunging NACA 0012 Airfoil. Drag-producing case at  $M_\infty = 0.2$  and  $Re = 1850$ . Time Spectral versus time accurate drag coefficients for  $N \in \{3, 9, 33\}$ . Ten periods of the rigid-motion time-accurate solution are plotted in red from steady-state startup. Blue squares and green diamonds locate the drag coefficient values at the Time-Spectral collocation points for relative- and rigid-body motion, respectively. Drag coefficient signals evaluated from reconstructed Time-Spectral solutions are plotted with hashed lines.

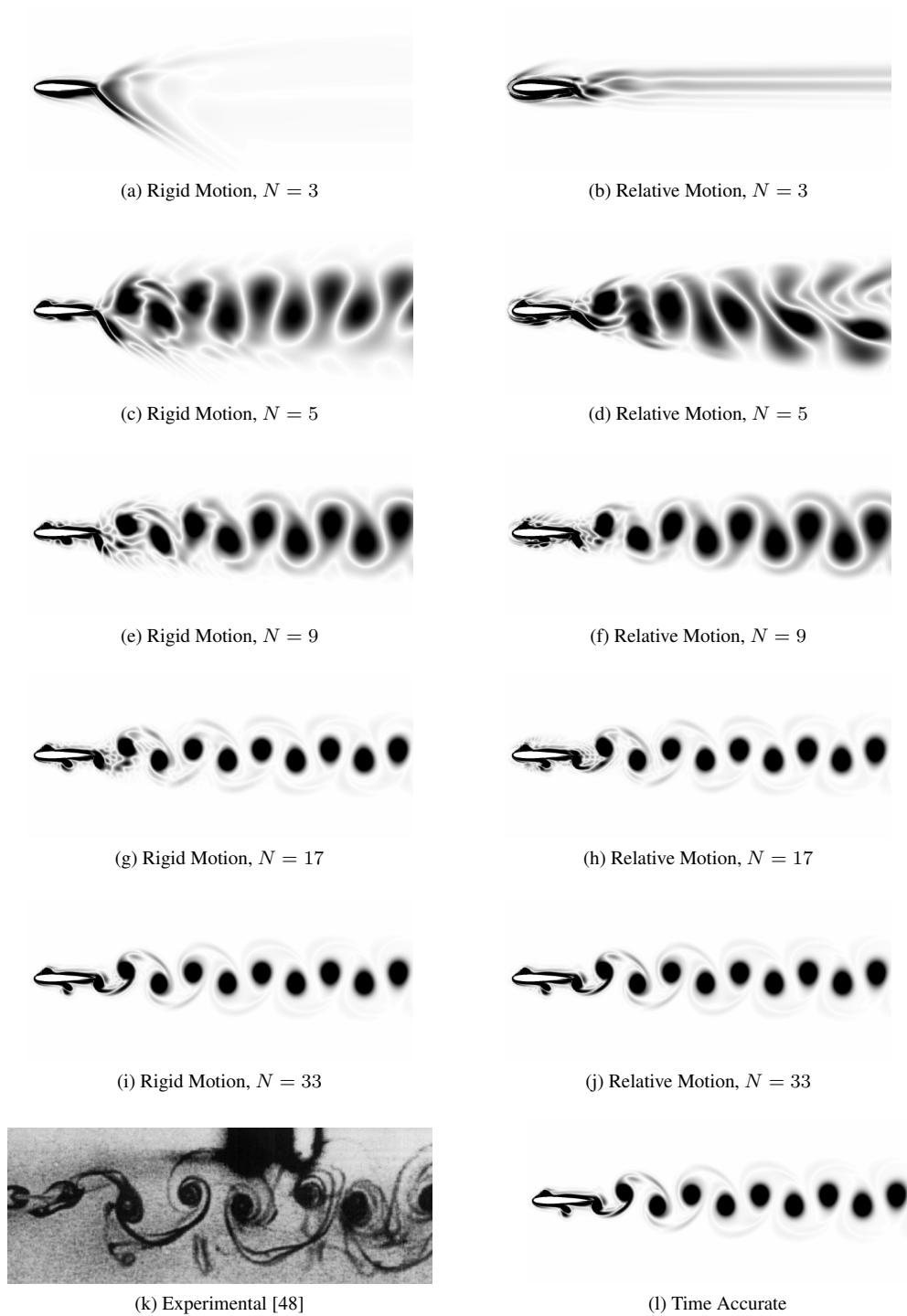


Figure 15: Laminar Plunging NACA 0012 Airfoil. Thrust-producing case at  $M_\infty = 0.2$  and  $Re = 1850$ . Visualization of vorticity magnitude. Comparison of experimental with computed time-accurate and Time-Spectral results using  $N \in \{3, 5, 9, 17, 33\}$  for both rigid- and relative-body motion.

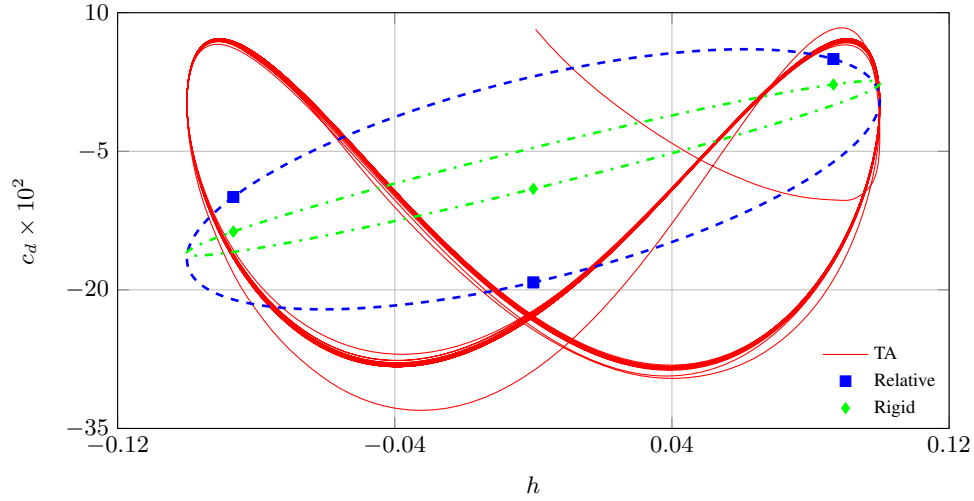
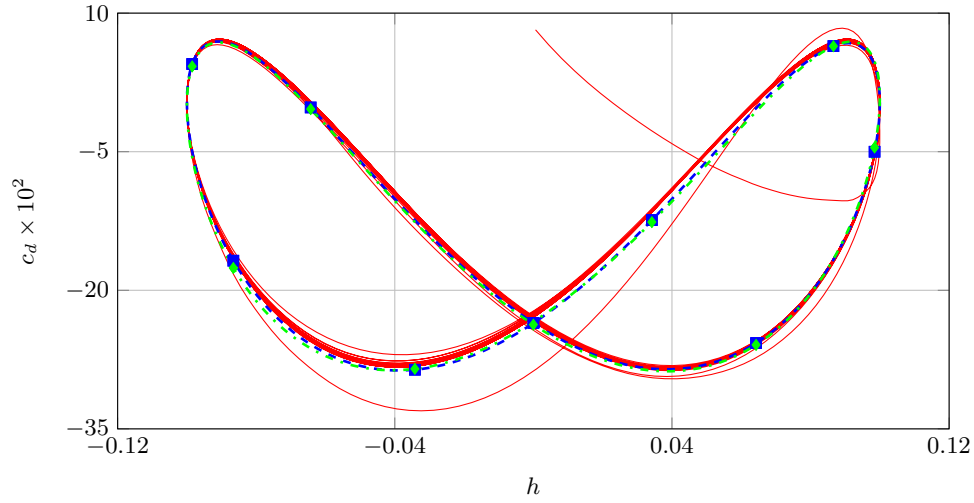
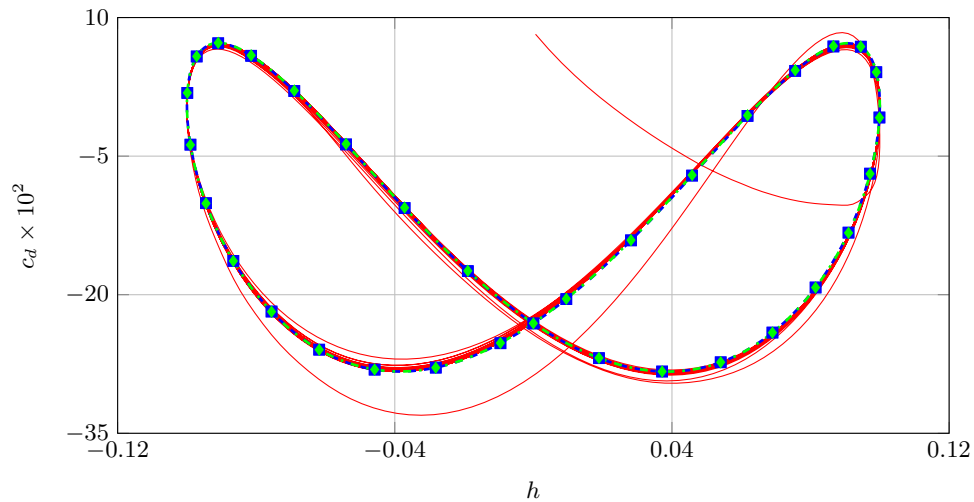
(a)  $N = 3$ (b)  $N = 9$ (c)  $N = 33$ 

Figure 16: Laminar Plunging NACA 0012 Airfoil. Thrust-producing case at  $M_\infty = 0.2$  and  $Re = 1850$ . Time Spectral versus time accurate drag coefficients for  $N \in \{3, 9, 33\}$ . The time-accurate solution is plotted in red from steady-state startup. Blue squares and green diamonds locate the drag coefficient values at the Time-Spectral collocation points for relative- and rigid-body motion, respectively. Drag coefficient signals evaluated from reconstructed Time-Spectral solutions are plotted with hashed lines.